UNIVERSITAT POLITÈCNICA DE CATALUNYA
BARCELONATECH
Centre de Formació Interdisciplinària Superior

UNIVERSITAT POLITÈCNICA DE CATALUNYA
BARCELONATECH
Escola Tècnica Superior d'Enginyeria
de Telecomunicació de Barcelona

telecos BCN

UNIVERSITAT POLITÈCNICA DE CATALUNYA
BARCELONATECH
Escola Superior d'Enginyeries Industrial,
Aeroespacial i Audiovisual de Terrassa

THE CATHOLIC UNIVERSITY OF AMERICA

Bachelor's Thesis

Analysis of Interplanetary Coronal Mass Ejections Observed by STEREO and MESSENGER

NASA Goddard Space Flight Center
Heliophysics Science Division (HSD)

Marina González Álvarez
May 2019

Degrees:
Grau en Enginyeria en Tecnologies Aeroespacials
Grau en Enginyeria Física

Advisors:
Dra. Teresa Nieves Chinchilla
Dra. Gloria Sala Cladellas

ABSTRACT

This thesis presents the work done by the author under the supervision of Dr. Teresa Nieves Chinchilla, in the Heliophysics Science Division of NASA Goddard Space Flight Center from September 2018 to February 2019.

In the first part, the most essential theoretical concepts on which space weather and ICME analysis build are explained. Thus, some essential ideas such as what CMEs and ICMEs are, different ways of detecting them, what type of effects these structures can have on our planet and the two most relevant missions for the study of ICMEs regarding the purpose of this work are detailed.

In the second part, a comprehensive analysis of a very particular event is presented after performing a classification and filtering of the totality of events observed by STEREO Ahead and Behind spacecraft within the time frame of 2013 to 2014. This final ICME of study (August 2013 - DOY 234) has been analyzed both from the in-situ and remote sensing perspectives, with the aim of connecting these two dimensions in an attemp to help better understand the internal magnetic structure of ICMEs. In this way, the different categories for in-situ classification are first detailed, followed by the corresponding characterization and filtering of events after adding the remote sensing observations to finally select the aforementioned structure for its comprehensive analysis due to its high inherent interest: firstly, the in-situ results together with their justification are developed; secondly, the three-dimensional reconstruction of the shape of the ICME by means of the Graduated Cylindrical Shell (GCS) model is presented; also, an implementation of some of the most relevant analytical models related to the study of ICMEs, such as the Circular-cylindrical and Elliptic-cylindrical Analytical Flux-rope Model for Magnetic Clouds are applied to the case of study; furthermore, the aforementioned analytical models are linked with the GCS implementation results to establish a comparison between the in-situ and remote sensing model implementations; finally, a speed analysis based on the GCS model results and the execution of the ENLIL model to verify some of the previous outcomes are presented. A publication of some of the results obtained in collaboration with the supervisors at NASA Goddard is currently under development.

Keywords: coronal mass ejection, flux rope, magnetic obstacle, solar wind

Contents

List of Figures

List of Tables

Acronyms

CC	Circular-cylindrical
CCAMMC	Circular-cylindrical Analytical Model for Magnetic Clouds
CCMC	Community Coordinated Modeling Center
CME	Coronal Mass Ejection
EC	Elliptic-cylindrical
ECAMMC	Elliptic-cylindrical Analytical Model for Magnetic Clouds
FR	Flux Rope
GCS	Graduated Cylindrical Shell
ICME	Interplanetary Coronal Mass Ejection
IPS	Interplanetary Shock
MC	Magnetic Cloud
MHD	Magnetohydrodynamics
MO	Magnetic Obstacle
WSA-ENLIL	Wang-Sheeley-Arge-ENLIL

Part I

Fundamentals of Space Weather

> You cannot look up at the night sky on the planet Earth and not wonder what it's like to be up there amongst the stars. And I always look up at the moon and see it as the single most romantic place within the cosmos.
>
> — Tom Hanks

1 | Introduction

Coronal mass ejections (CMEs) expelled from the solar corona are a major space weather driver, both in space and on the ground. The fast-traveling CME plasma, which carries a twisted magnetic field, is a common source of geomagnetic disturbances that can affect a wide range of human technologies. Thus, understanding the magnetic structure and dynamics of CMEs is of critical importance for space weather forecasting.

As society's reliance on technological systems grows, so does our vulnerability to space weather. The ultimate goal in studying space weather is an ability to foretell events and conditions on the Sun and in near-Earth space that will produce potentially harmful societal and economic effects, and to do this adequately far in advance and with sufficient accuracy to allow preventive or mitigating actions to be taken.

Thanks to the past and current Heliophysics System Observatories (HSOs), we have advanced our understanding by, for instance, connecting the traditional 'magnetic clouds with the CMEs. However, our proficiency in unraveling the internal magnetic structure of their counterpart in the interplanetary medium, the ICMEs, is still limited. The goal of this work is to decipher the internal magnetic configuration of several ICMEs observed by STEREO and MESSENGER by systematically sorting, studying, and quantifying the internal magnetic structure.

In order to do that, a characterization of the events observed by the aforementioned spacecraft during the time interval of 2013 to 2014 (maximum of solar cycle 24) has been made. Also, a final ICME that presents the most interesting internal structure based on the in-situ results and source region images is selected for multipoint observation measurements and 3D multi-view reconstruction analysis in an attempt to help establish a link between in-situ and remote sensing observations.

2 | Covering the basics of ICMEs

2.1 What is a CME? And an ICME?

We live in the era of nanoelectronics and space technology. We are being witnesses of massive technological advancements, such as how we can now store large amounts of data that 40 years ago easily occupied an entire building in a little pen drive of the size of a thumbnail. While the need for smaller and faster electronics provides technical obstacles, the natural environment imposes its own difficulties and, more often than not, these are much harder to interpret, understand and, therefore, predict. However, during the last three decades there have been major discoveries within the field of space science and space weather that have allowed us to understand the important concept of what a CME is and how it can affect our technology both orbiting the Earth and on the planet.

As stated in [6], a CME or coronal mass ejection, is a large eruption of plasma and magnetic field from the Sun. It can contain a mass larger than 10^{13} kg and may achieve a speed of several thousand kilometers per second. A typical CME has a mass of around $10^{11} - 10^{12}$ kg and has a speed between 400 and 1000 km/s. It also typically spans several tens of degrees of heliographic latitude (and probably longitude). By comparison, the Earth has a mass of around $6 \cdot 10^{24}$ kg and is around $(5 \cdot 10^{-3})^\circ$ in heliographic latitude (see Figure 2.1).

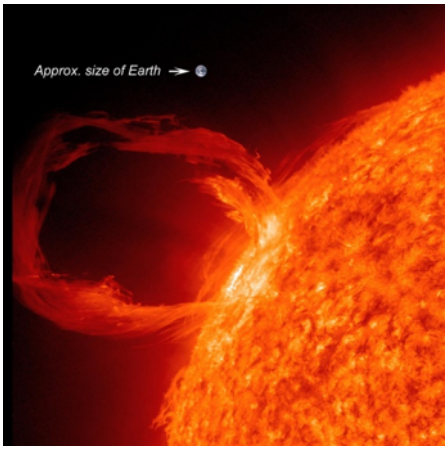

Figure 2.1: Comparison between the size of a CME vs. planet Earth. Figure from [11].

The occurrence with which CMEs erupt from the Sun is mainly related to the solar cycle, which lasts about eleven years each. Thus, it is often possible to observe an

occurrence of four or five CMEs a day during typical solar maximum, in contrast to around only one CME a day during solar minimum. Moreover, the majority of the CMEs that erupt from the Sun are not directed towards the Earth.

When a CME reaches distances that are very far away from the Sun ($> 50R_s$) it is possible to talk about ICMEs or interplanetary coronal mass ejections (see Figure 2.2). Thus, ICMEs are generally regarded as the heliospheric counterpart of the CMEs and, although they share the same type of internal magnetic structure and have a large mass, they are usually slower. However, they still tend to travel at supersonic speeds (faster than the speed of sound in the surrounding solar wind) through the interplanetary medium, causing very characteristic shocks that help categorize each type of event, as it will be further explained in Section 3.1.

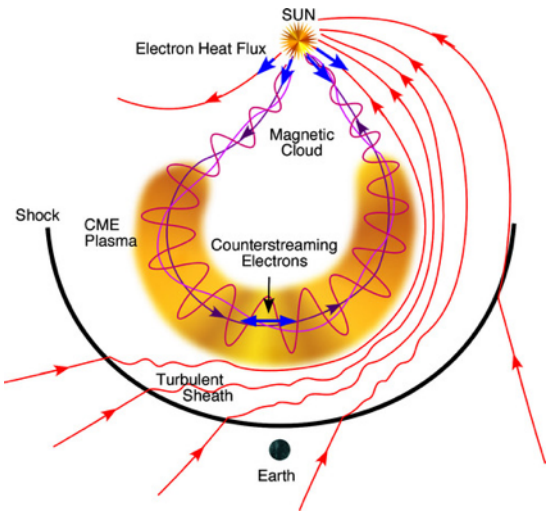

Figure 2.2: Structure of an Interplanetary Coronal Mass Ejection (ICME). Figure from https://eclipse2017.nasa.gov/coronal-mass-ejections.

2.2 How CMEs and ICMEs are detected

There are two main ways in which coronal mass ejections can be detected: by means of in-situ measurements or through remote sensing observations. Basically, the first type of detection corresponds to the measurements of many different parameters such as magnetic field, solar wind density or velocity that are taken when the structure crosses any of the spacecraft aimed for this purpose. Thus, the spacecraft actually "touches" the solar wind and collects data corresponding to the CME's properties and configuration. Later in this work, a detail explanation related to the graphs shape and results interpretation derived from the in-situ observations will be provided in Section 3.1.

On the other hand, the remote sensing detection modality consists in taking pictures of CMEs from the distance. In this way, a special device specifically developed for this purpose must be used in order to actually be able to observe the eruptions: the coronagraphs. These appliances block out most part of the light that comes from the Sun, leaving only the relatively faint surrounding corona. There is a challenging issue, however, that must be addressed: coronagraph images are two-dimensional, so

that photos of CMEs are in fact projections into the sky plane. This issue makes it sometimes difficult to determine the actual shape and trajectory of the CME. There are nevertheless two different categories of CMEs that can be easily recognized:

- Large component along the Sun-observer line (see Figure 3.12): those structures heading directly toward or away from the observer. These types are referred to as partial halo or halo CMEs, as they appear to partially or totally encircle the Sun, respectively. This first category is the one that results more interesting for the purposes of this work.
- Minor component along the Sun-observer line (see Figure 3.11): in this case the CME does not head towards the observer and its size, speed or direction properties are, usually, more easily identifiable.

Due to the problems posed by projection into the sky plane, it is commonly useful to have a look at solar surface eruptions right on the solar disk such as solar flares, disappearing filaments or erupting prominences, among others; as they usually provide the observer with notable clues about the way the eventual CME will propagate (see Figure 2.6, 2.7, 2.8 and 2.9).

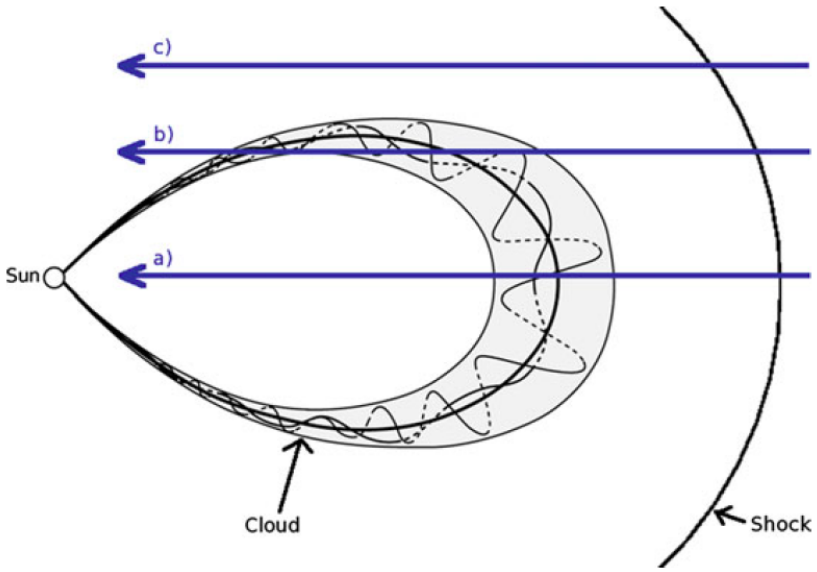

Figure 2.3: Scheme demonstrating confusion in using in-situ data results to measure ICMEs. Three spacecraft tracks are shown through a single ICME structure, including the shock and sheath regions: (a) Passing through the centre, (b) crossing through a flank, and (c) passing through the sheath region but missing the cloud entirely. In cases (b) and (c) it is difficult to know whether the ICME contained the magnetic structure or not. Figure from [6].

There is one disadvantage, however, that the in-situ measurements present over the remote sensing observations: the fact that they are only capable of monitoring a single track through the ICME as it crosses the spacecraft. Thereby, this kind of measurements provides the observer with incomplete information about the structure and composition of ICMEs and can lead to confusion. For example, it often occurs that the ICMEs observations are not associated with magnetic clouds and a clear question arises here: is this because the ICMEs is not really related to a MC or maybe because we are only "seeing" a fraction of the entity which makes our observations to be mistaken (see Figure 2.3)?

2.3 Effects of ICMEs on planet Earth

Increase in radiation exposure to high-altitude aircraft fliers and astronauts, potential crash landing due to an increment in atmospheric drag on orbiting spacecraft, interference in spacecraft circuitry, telecommunication or hardware damage are just some examples of the many devastating effects in which ICMEs can affect human's technology. In this way, the study of space weather is essential not only from a scientific point of view, but for technical interests as well, in order to be prepared to minimize the consequences of the negative impact of ICMEs on Earth. So, how can ICMEs actually produce such deleterious effects?

In order to crystallize the process through which ICMEs affect our planet, it is necessary to talk about how the solar wind, which can be understood as an ocean of magnetic field and plasma that is continuously flowing outward from the Sun, is distorted by the geomagnetic field and vice versa, causing a phenomenon widely known as *magnetic reconnection*.

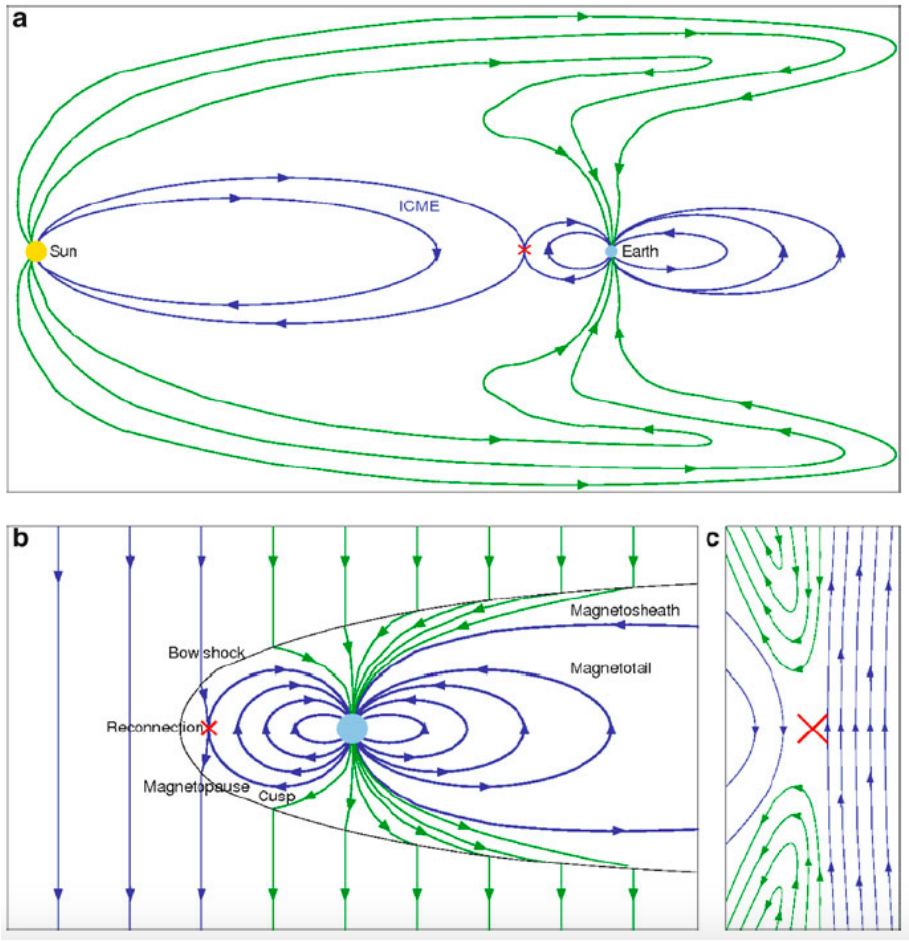

Figure 2.4: Simplified scheme of magnetic reconnection on the dayside equatorial plane of the Earth's magnetosphere. a) Representation of the interplanetary magnetic field and ICME that passes through the Sun and the Earth (green) and the ones that are connected only with the Earth or the Sun (blue color). b) A close-up view of the Earth's magnetosphere. c) Close-up view of the reconnection site on the dayside. Figure from [6].

Taking into account that the geomagnetic field is always directed northward, two different possibilities can be encountered (see Figure 2.4):

1. The direction of the ICME's magnetic field, which from the Earth's perspective can be described as a denser version of the solar wind, is northward. In this case, there is no interference in arrival between the geomagnetic and the ICME's field lines, so that no magnetic reconnection takes places on the dayside of the Earth. It can still happen on the nightside, but the effects for this case are very subtle, not leading to magnetic storm conditions.

2. The solar wind's field lines direction is southward; this is, opposite to that of the Earth's. This phenomenon causes the field lines of the cusp region (near the poles) to open and being, thus, no longer connected to each other but to the interplanetary magnetic field (see Figure 2.4b and c). During this process, the southward-directed magnetic field that arrives at the magnetosphere temporarily connects to that of the Earth's, causing the event denoted as magnetic reconnection. Once magnetic reconnection takes place, more and more field lines on the magnetosphere's dayside start to open, so that the cusp moves slightly towards the equator. This divergence of the magnetic field lines near the poles allows particles from the solar wind to enter the atmosphere causing, for example, the northern lights to occur when these particles finally precipitate or the aforementioned negative effects on human's technology and the Earth.

2.4 Missions for the study of ICMEs

A myriad of missions aimed to explore CMEs have been developed during the last decades. In this section, some of the most important ones which are, subsequently, the most relevant for this work, are explained.

2.4.1 STEREO

The Solar TErrestrial RElations Observatory is the third mission in NASA's Solar Terrestrial Porbes Program, which provides missions to understand the fundamental physics processes from the Sun to the Earth, to outer planets and beyond the interstellar medium. It employs two nearly identical space-based observatories widely known as the *twin spacecraft* to provide the first-ever stereoscopic measurements to study the Sun and the nature of its coronal mass ejections.

The twin STEREO spacecraft were launched on October 25$^{\text{th}}$, 2006 from Cape Canaveral Air Force Station in Florida. The observatories were ejected from Earth orbit in the opposite directions (see Figure 2.11), so that STA takes 347 days to complete one revolution of the Sun (A/Sun/Earth angle increases at 21.650 °/year) and STB 387 days (B/Sun/Earth angle increases at 21.999 °/year). Although the STEREO mission design lifetime was two years, the STA observatory continues operating as expected and taking science data on a regular basis. Communications with STEREO Behind were nonetheless lost on October 1$^{\text{st}}$, 2014 due to multiple

hardware anomalies affecting control of the spacecraft orientation. After many recovery attempts with the observatory –some of them successful, although most futile- NASA stated the official cease of the spacecraft on October 17th, 2018. Despite the contact loss with STB in 2014, STEREO mission has been and will continue to be providing robust solar research in the upcoming years, entering its second decade of operations and delivering far beyond expectations.

STEREO provides a unique and revolutionary view of the Sun-Earth system by helping unraveling the 3D structure of coronal mass ejections and responding the still unanswered question of *why do they occur*. In this way, the STEREO's scientific objectives are to: understand the causes and mechanisms of CMEs initiation, characterize the propagation of CMEs through the heliosphere, discover the mechanisms and sites of energetic particle acceleration in the low corona and the interplanetary medium and, finally, improve the determination of the structure of the ambient solar wind.

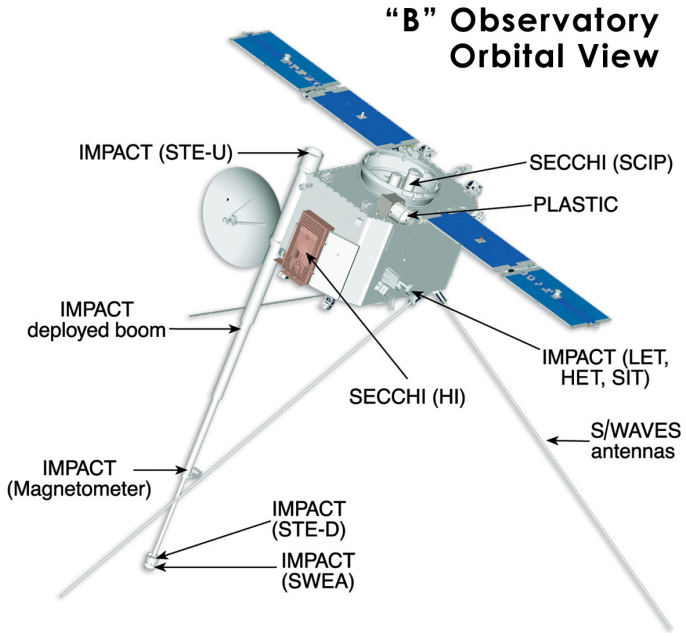

Figure 2.5: A close-up of the STEREO spacecraft body showing the SECCHI Sun Centered Instrument Package, the IMPACT and PLASTIC instruments, a number of other instruments and spacecraft subsystems. Figure from [11].

The spacecraft bus consists of six operational subsystems supporting two instruments and two instrument sites, which provides a total of sixteen instruments per observatory. The most relevant instruments used in this work are:

- The SECCHI EUVI - Extreme UltraViolet Imager (LMSAL): aimed to resolve the CME's initiation and early evolution by providing 171Å, 195Å, 284Å and 304Å ultraviolet light images. The most remarkable features that can be observed thanks to the EUV imager are the bright active regions, coronal holes and long thin prominences (see Figures 2.6, 2.7, 2.8 and 2.9).
- The SECCHI COR1 - Inner Coronograph (GSFC): a classic Lyot internally occulting refractive coronograph, adapted for the first time to be used in space. The field of view is from 1.3 to 4 solar radii (see Figure 2.10a).

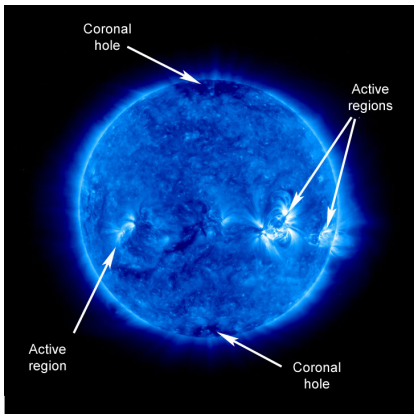

Figure 2.6: The Sun at 171Å. Light at this wavelength is chiefly emitted by Fe IX and X (iron ionized 8 or 9 times) at 1.0 million degrees K. Figure from [11].

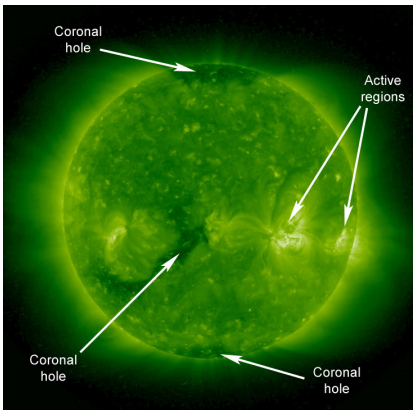

Figure 2.7: The Sun at 195Å. Light at this wavelength is chiefly emitted by Fe XII (iron ionized 11 times) at 1.4 million degrees K. Figure from [11].

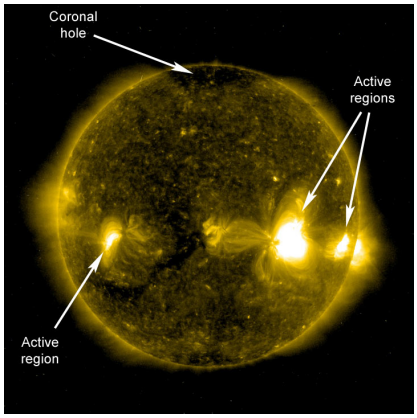

Figure 2.8: The Sun at 284Å. Light at this wavelength is emitted by Fe XV (iron ionized fourteen times) at 2.2 million degrees K. Figure from [11].

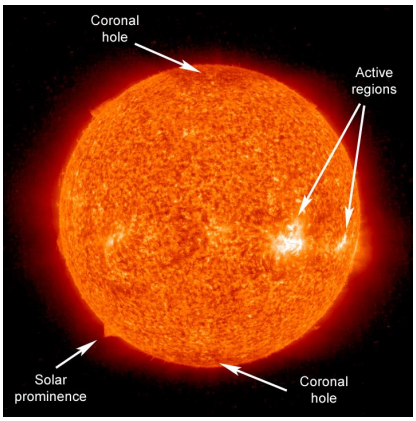

Figure 2.9: The Sun at 304Å. Light at this wavelength is emitted by He II (helium ionized once) at 60000 - 80000 degrees K. Figure from [11].

- The SECCHI COR2 – Outer Coronograph (NRL): the COR2 detectors observe a range from 2.5 to 15.6 solar radii (see Figure 2.10b).

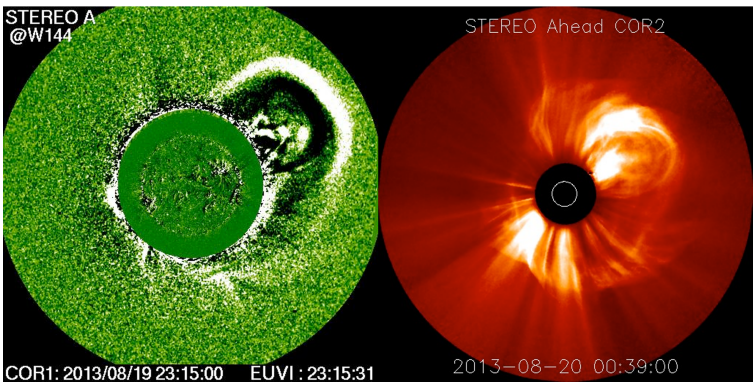

Figure 2.10: a) Image of the sun taken by the SECCHI COR1 coronograph (left). b) Another image corresponding to the same event, observed this time by the SECCHI COR2 coronograph (right).

- The IMPACT – In-Situ Measurements of Particles and CME Transients: a suite of seven instruments that samples the 3D distribution of solar wind plasma electrons, the characteristics of the solar energetic particle (SEP) ions and electrons and the local vector magnetic field.
- The PLASTIC – Plasma and Suprathermal Ion Composition: sampling of the solar wind and suprathermal particles, providing measurements of kinetic particles and composition.

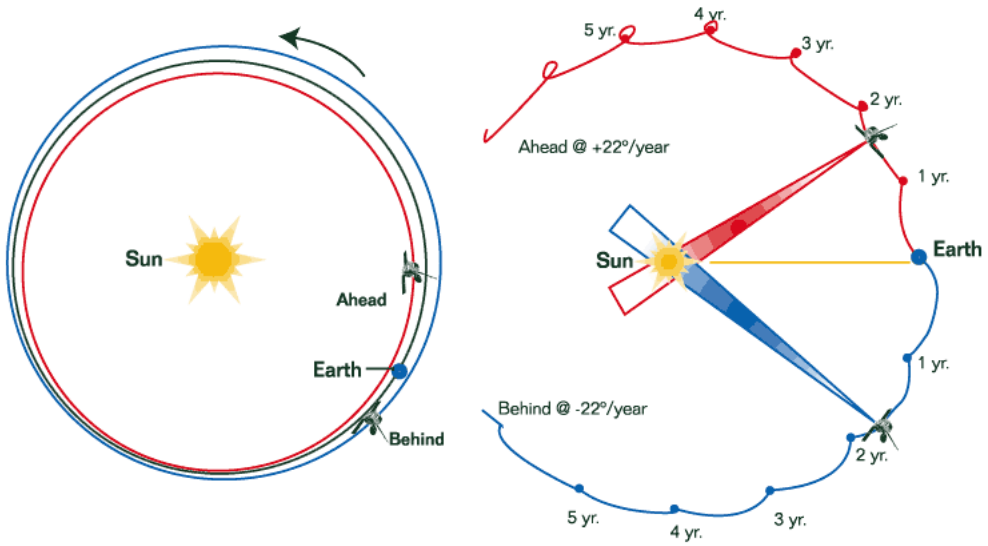

Figure 2.11: Orbits of the STEREO Ahead (red) and Behind (blue) observatories relative to the Earth's orbit (green). Figure from [11].

2.4.2 MESSENGER

The objective of NASA's MErcury Surface, Space ENvironment, GEochemistry and Ranging mission (MESSENGER) was to map the surface composition, study the magnetic field and interior structure of planet Mercury. The spacecraft became the first one ever to orbit the planet on March 18th, 2011 and successfully continued operating until four years later. It was not until April 30, 2015, when it impacted the surface of Mercury at a speed of more than 3.91 kilometers per second, marking the end of operations for the hugely successful mission.

The most relevant instrument of the nine carried by the spacecraft that is notable to mention for the purpose of this work is the MAG or Magnetometer. This device was aimed to investigate the structure of Mercury's magnetic field and its interaction with the solar wind.

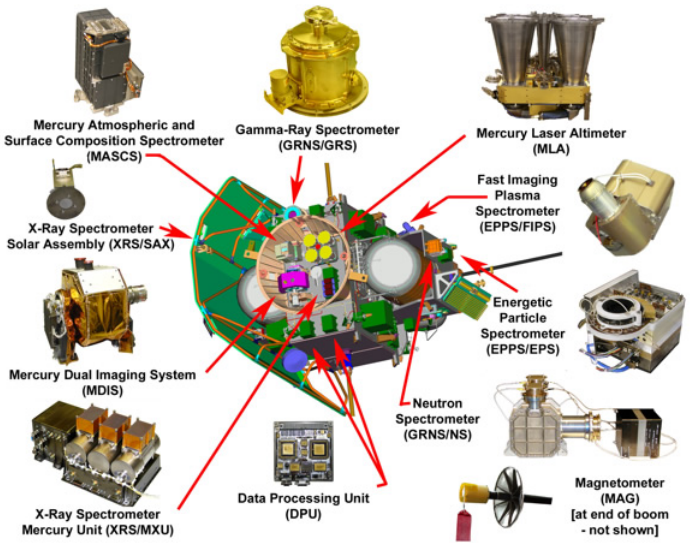

Figure 2.12: A close look of the MESSENGER spacecraft body and all its instruments and subsystems. Figure from [11].

Part II

Categorization of events and analysis of a very particular ICME

> Remember to look up at the stars and not down at your feet. Try to make sense of what you see and wonder about what makes the universe exist. Be curious.
>
> — Stephen Hawking

3 | Events classification and filtering

3.1 In-situ data analysis and categorization techniques

Coronal mass ejections (CMEs) are eruptions of magnetized plasma from the solar corona into the heliosphere, which are commonly observed via imaging instruments, such as white-light coronagraphs. Their interplanetary signatures, so-called interplanetary coronal mass ejections (ICMEs), are usually detected via in situ instrumentation with specific imprints on the observations. Sometimes, following an interplanetary shock, we observed a period of a magnetic field with low proton temperature that was stronger than the ambient field, a relatively quiet and smooth rotation of the magnetic field, a helium abundance enhancement, and/or bidirectional electrons. The in situ measured properties of ICMEs ([23], [7]) in interplanetary space do not necessarily reflect the initial solar conditions and/or magnetic field structure ejected at the Sun.

An example of the behavior of the different in-situ measurement parameters can be observed in Figure 3.1: magnetic field magnitude, magnetic field components (in RTN coordinate system), proton number density, proton thermal speed and proton beta, solar bulk flow speed. There are three main parts that can be identified in the observations of an event that must be highlighted:

1. **ICME Start Time** (black vertical line in Figure 3.1): this time is selected using the interplanetary shock, which is characterized by a sudden change and, therefore, a remarkable discontinuity in the different parameters' values.

2. **Sheath** (interval between the first black and green vertical lines in Figure 3.1): after the IPS (interplanetary shock) comes the sheath, which consists of heliospheric plasma and magnetic field and it is an interval where fluctuations of the parameters which do not respond to any kind of pattern. This time is marked along with the increase in magnetic field and plasma parameters (proton density, temperature, and speed), or, in the case of no clear signatures, the ICME start time will coincide with the *magnetic obstacle* (MO) start time.

3. **Magnetic Obstacle (MO)** (interval between green lines in Figure 3.1): an increase of the magnetic field magnitude and the solar bulk flow speed and a diminution of the rest of the parameters are commonly observed along the MO interval. Moreover, the value of the β_{proton} variable, which is defined as the

quotient between the thermal and the magnetic pressure, presents a marked decline as the dominant pressure inside the CME is undoubtedly magnetic.

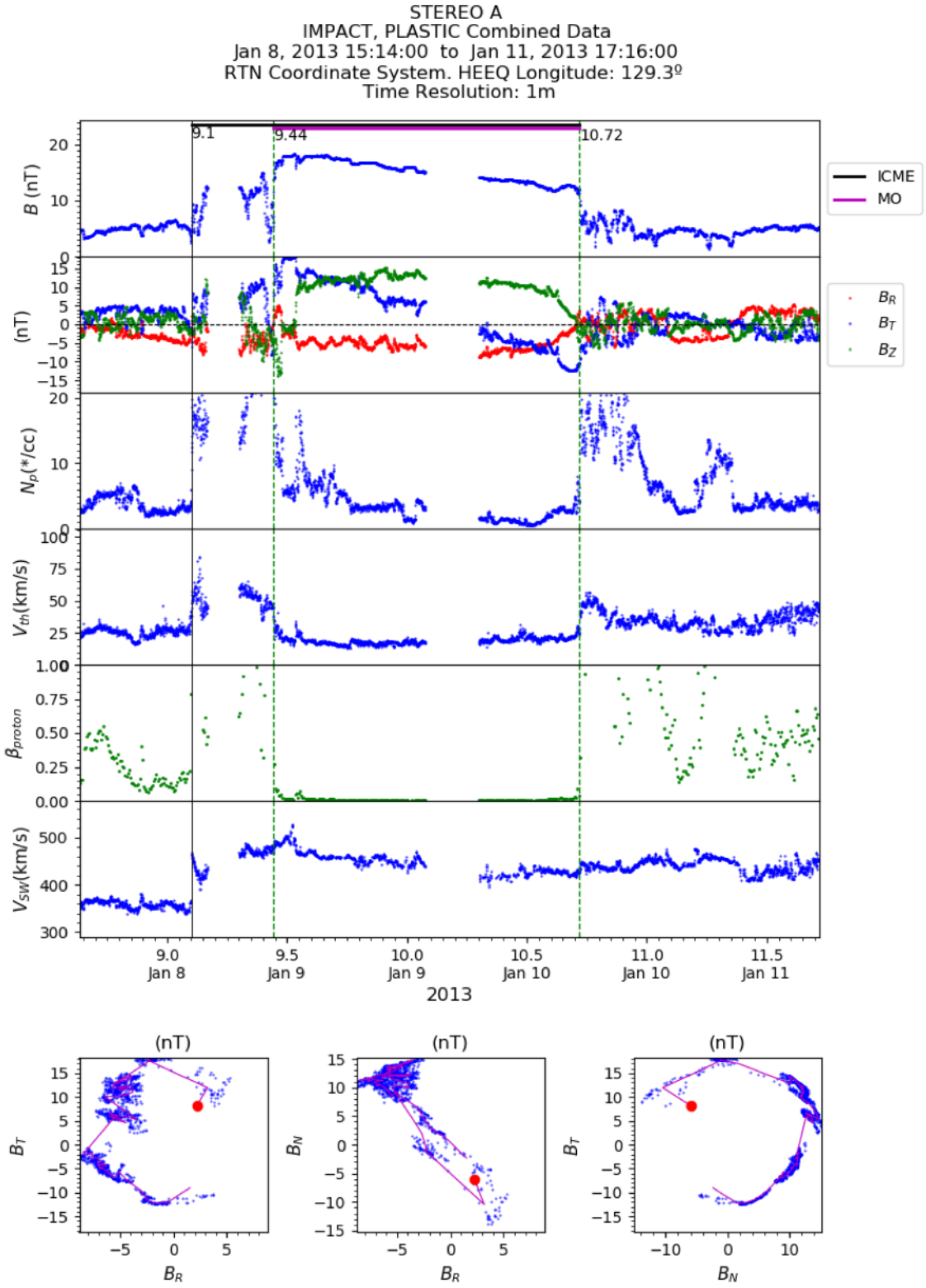

Figure 3.1: Graphical representation example of the in situ data from the IMPACT and PLASTIC instruments onboard the STEREO A spacecraft on January 8-11, 2013. From the top, the magnetic field magnitude and components in the RTN coordinate system, proton plasma density, temperature (expressed as a thermal velocity), proton beta and solar wind speed. The vertical lines show the interval of the ICME front and MO boundaries. (b) Three combined magnetic hodograms in RTN coordinate system.

Finally, the last three subplots are used to better understand the nature of the magnetic field components' rotation in order to be able to classify the kind of MO for each event in the most accurate possible way. These graphs are commonly referred to as the magnetic field *hodograms*. The pink line that appears on these plots is an hourly average that allows to more easily understand the tendency and behavior of the magnetic field rotation. The red point just refers to the first average point within the MO interval, so that the direction of the rotation –northward or southward- can be inferred.

The MOs are intervals that can be classified attending to three possible types of configurations:

- **Flux rope (F)**: organized magnetic topology. When there are clear in-situ signatures, smooth and large magnetic field rotations are often observed. In Figure 3.2 a very clear example of this kind of structure is presented. First, the ambient, unperturbed solar wind with low, almost constant values of the magnetic field magnitude is detected. Then, right before Dec 2, a sudden change in both the magnitude and components of this parameter indicates the arrival of an IPS and, thus, the start time of the ICME that is being detected by STEREO Ahead. Right afterwards, random fluctuations of B take place up until a point where the magnetic field changes its unpredictable behavior for a quite, smooth and continuous one. In this way, very well-defined rotations of B_N vs. B_R and B_T vs. B_N are observed during the whole duration of the MO interval, both in the magnetic field's components global graph and in the hodograms.
- **Complex (Cx)**: when a change in the natural comportment of the parameters, leading to two or more linked configurations takes place. These structures display irregular in-situ signatures that are possibly due to the interaction between successive CMEs. In the case of Figure 3.3, a behavioral change in the parameters is detected at around DOY 175.75. Thus, a first northward rotation, highlighted in blue, and a second southward rotation, marked in orange, are observed, leading to two different linked configurations.
- **Ejecta (E)**: when there is no ordered topology or monotonic change in the magnetic field. In this final case (see Figure 3.4), an IPS followed by the sheath and its characteristic fluctuations are detected, but no distinguishable behavioral pattern of the magnetic field is observed.

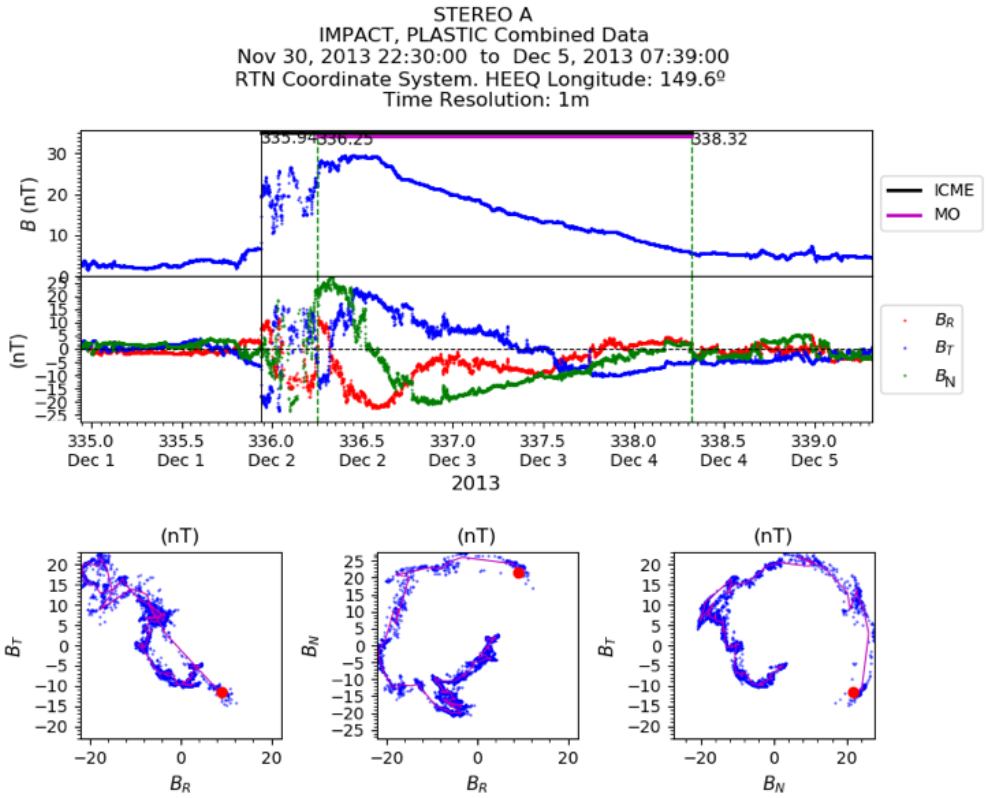

Figure 3.2: Example of a flux rope (FR) MO configuration type. In situ data obtained from the IMPACT instrument onboard the STEREO A spacecraft on December, 2013.

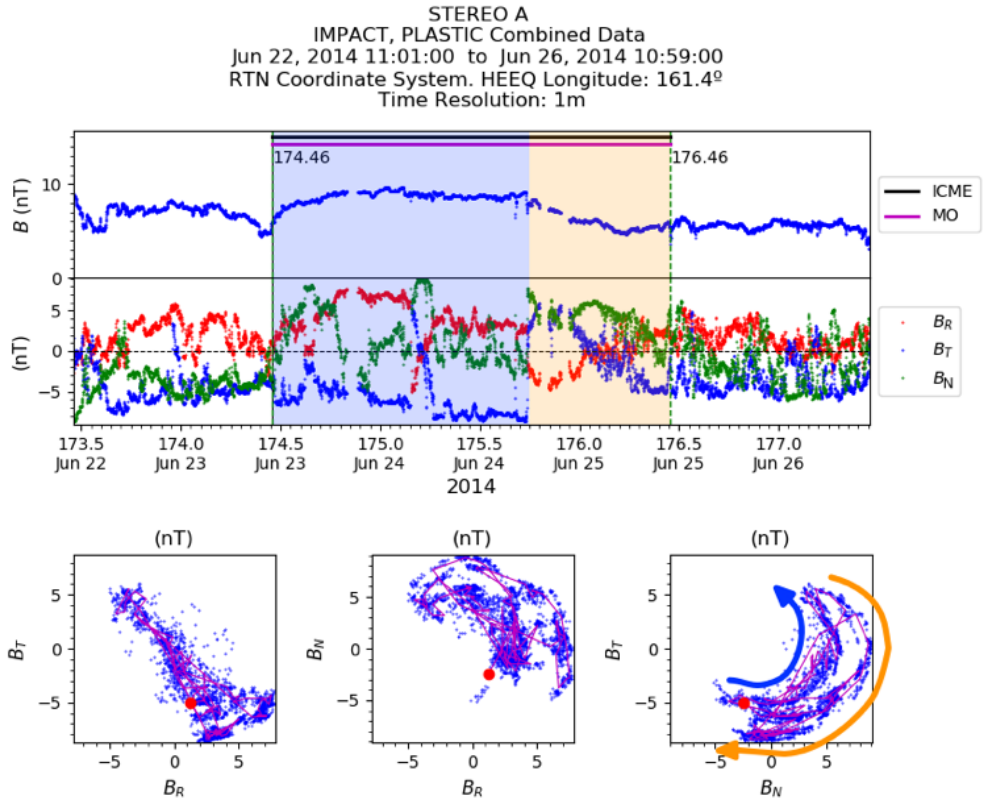

Figure 3.3: Example of a complex (Cx) MO configuration type. In situ data obtained from the IMPACT instrument onboard the STEREO A spacecraft on June, 2014.

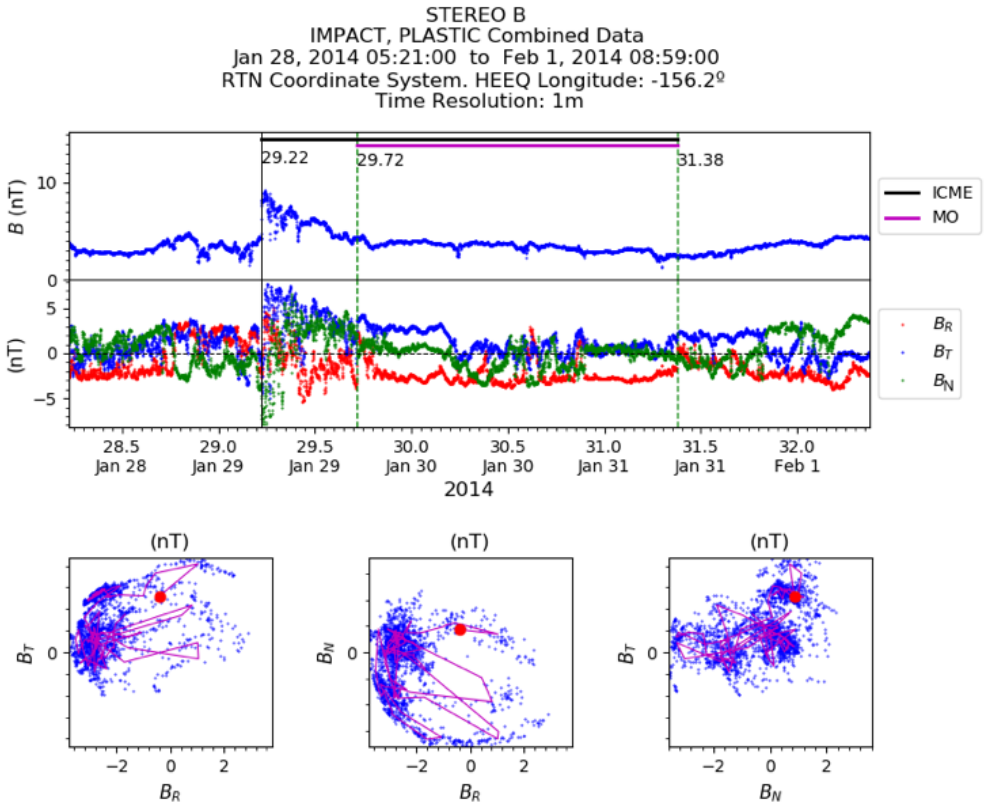

Figure 3.4: Example of an ejecta MO configuration type. In situ data obtained from the IMPACT instrument onboard the STEREO A spacecraft on January, 2014.

3.2 Filtering of events based on remote and in-situ measurements

3.2.1 Characterization of the events

As stated in Section 1, the aim of this work is to find an interesting event between 2013 and 2014 that is suitable for both multipoint and multi-view observation analysis by the STEREO spacecraft Ahead and Behind and/or MESSENGER in an attempt to establish a link between in-situ and remote sensing observations to better understand the internal magnetic structure of an ICME. The first step to accomplish this goal is to perform a characterization of all the events that pertain to the 2013 - 2014 time frame, by following the nomenclature and categories explained in the previous section.

Since the launch of the STA and STB, a continuous monitorization of the solar wind, large-magnetic structures, shocks and solar energetic proton events has been made at the Heliospheric Science Division at NASA GSFC. Thus, the information regarding the ICME's start and end date for both spacecraft during the time period of interest has been obtained from the *Level 3 Results of STEREO IMPACT/PLASTIC ICMEs List*, compiled and maintained by Lan Jian at NASA Goddard[1]. This useful list of events has been used as an input to obtain the in-situ results presented at this work, that have led to the classification enclosed in Table A.1. A little sample of these results can be seen in Table 3.1.

STEREO A		STEREO B	
2013 009 010/9 02:25	F+		
2013 025 01/25 00:14	F		
2013 039 02/08 07:44	E	2013 039 02/08 08:20	F-
2013 050 02/19 07:44	F	2013 049 02/18 03:06	E
2013 059 02/28 21:14	E		
		2013 066 03/07 12:23	E
2013 067 03/08 02:20			
		2013 083 03/24 05:20	Cx
...	...	...	...

Table 3.1: Sample of some of the events of study and their corresponding in-situ classification.

Thus, in Table A.1, all the different events and their corresponding category –flux rope, complex or ejecta- are provided. Each of the events detected by STA that is no more than three days apart from another detection corresponding to STB, or vice versa, is a candidate for multipoint observations and so, is located in the same row as the latter.

Finally, after carefully reviewing the totality of the events, the ones that are the best candidates for multipoint observations based on their configuration and how close in time they are detected by both spacecraft are selected for the continuation of the study. These events are summarized in Table 3.2.

[1] http://www-ssc.igpp.ucla.edu/forms/stereo/stereo_level_3.html

STEREO A		STEREO B	
2013 171 06/20 11:13	F	2013 170 06/19 15:08	Cx
2013 234 08/22 07:05	Cx	2013 234 08/22 02:10	E
2013 308 11/04 08:56	Cx	2013 309 11/05 02:43	Cx
2014 036 02/05 03:27	Cx	2014 036 02/05 16:05	Cx
2014 058 02/27 20:46	E	2014 059 02/28 04:23	E
2014 101 04/11 15:24	F-	2014 102 04/12 02:27	F+
2014 160 06/09 09:30	F-	2014 160 06/09 01:18	F+
2014 223 08/11 09:03	F	2014 223 08/11 06:20	Cx

Table 3.2: Small contingent of events that are most likely to have been both detected via multipoint in-situ measurements and remote sensing observations by both STEREO spacecraft in 2013 and 2014.

Thus, all these events are, a priori, good candidates for the purpose of this work so that, in order to select the ultimate event for study, further analysis -presented in the upcoming sections- is needed.

3.2.2 Source region description and remote sensing observations

Once the in-situ analysis of the events has been performed, the next necessary step that needs to be taken in order to identify the ultimate ICME candidate that has been both observed and detected by STA and STB is to do a remote sensing analysis. In order to do this, the *LASCO CME Catalog*[2] provided by the Heliophysics Science Division (HSD) of NASA GSFC has been used.

The aforementioned catalog provides continuous images of the Sun, as it is observed by the STEREO spacecraft while they orbit around the star. In this way, there are mainly six different types of images available that are contingent upon the instrument that takes each of the pictures (see Section 2.4.1): EUVI 171, EUVI 195, EUVI 284, EUVI 304, COR1 and COR2.

Taking into account that the aim now is to double check which of the events do actually cross the spacecraft in-situ via multipoint observations, the first step is to use the EUVI imagers to look for ICMEs that occur as close as possible to the Sun equator. This will likely increase the probability that the analyzed ICME is headed directly towards STEREO.

Moreover, it is always interesting to try to identify solar filaments on the disk surface to have a clue of the approximated longitude, latitude and tilt angle of the CME in the moment that it is ejected from the Sun. Solar filaments are clouds of ionized gas above the solar surface squeezed between magnetic regions of opposite polarity. Being cooler and denser than the plasma underneath and their surroundings, they appear as dark lines when seen on the solar disk. An example of a solar filament is shown in Figure 3.5.

Taking all this information into account, a remote sensing analysis of some of the

[2]https://cdaw.gsfc.nasa.gov/CME_list/index.html

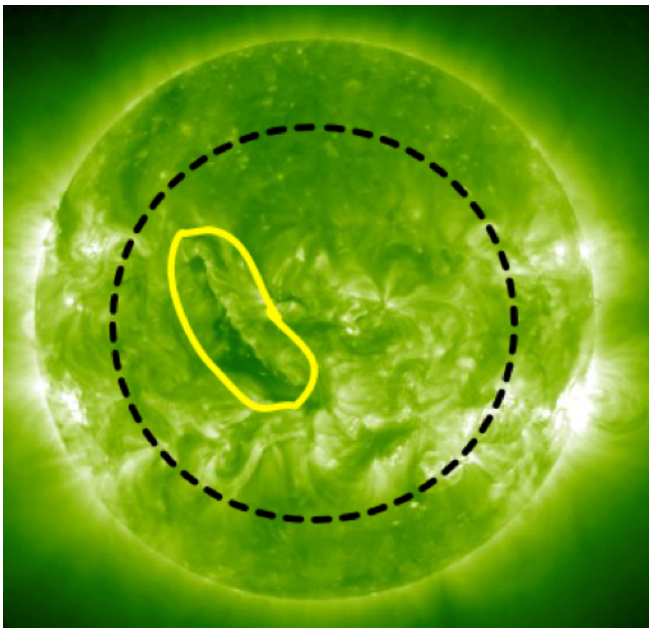

Figure 3.5: Example of a solar filament on the disk surface of a EUVI 195Å image (highlighted under a yellow line). The discontinuous black circumference delimits the approximated area where the appearance of these filaments is more likely to fulfill the condition of finding an ICME for multipoint in-situ measurements.

events presented in Table 3.2 will now be presented to show the working methodology for the selection of the final event. Specifically, the second, forth and sixth event presented in the aforementioned table are studied in chronological order. In Figure 3.6 the trajectory of the STEREO twin spacecraft during the timeframe selected for this study –maximum of solar cycle 24: years 2013 and 2014- is shown.

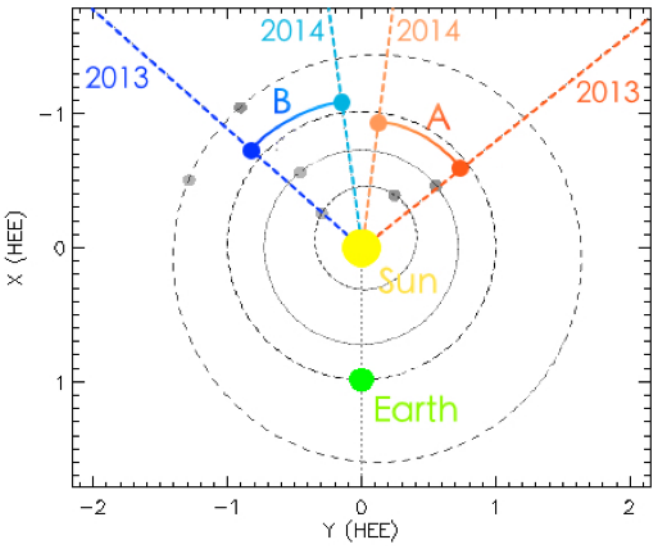

Figure 3.6: Evolution of the trajectory of the STEREO spacecraft within the time frame Jan 2013 - Dec 2014.

1. **Event 1: August 2013**
   First of all, the CME detected by STA on the 2013 234 08/22 07:05 and STB on the 2013 170 06/19 15:08 will be analyzed. In Figure 3.7 the angular location and separation angle of the spacecraft is shown. Furthermore, Figure 3.10 shows the images taken by EUVI 195, COR1 and COR2 that correspond to the event of study. The yellow circle that has been added to both EUVI images indicates the exact place from which the CME is first ejected, which corresponds to the brightest area inside the circles (active region). This CME's birth spot is very close to the Sun's equator and directed almost at the same angular separation from both STEREO, which makes it a good candidate for multipoint observations, even if the spacecraft present a non-negligible separation angle of 77.9 degrees. Also, even in hypothetic case that the CME would only cross one of the STEREO due to the large distance between the observatories at the time of detection, it would always cross MESSENGER (represented by planet Mercury in the scheme); so that this event is a very good candidate for both multi-point (STEREO A and/or B + MESSENGER) and 3D multi-view (STEREO A and B) observations.

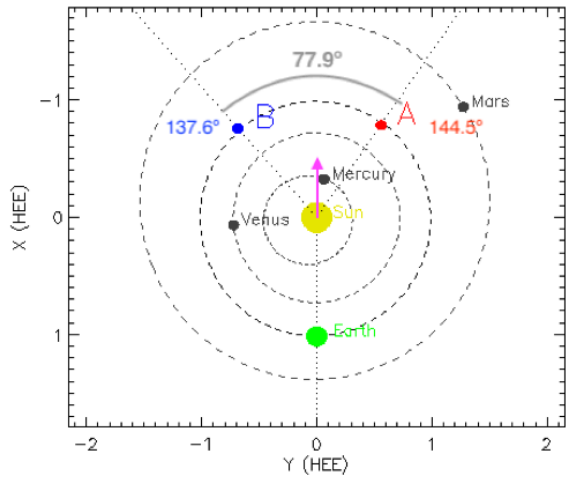

Figure 3.7: Simplified depiction of the relative position between the STEREO spacecraft, MESSENGER and the ICME being ejected in August, 2013 (DOY 234).

2. **Event 2: February 2014**
   On the other hand, the event detected by STA on the 2014 036 02/05 03:27 and STB on the 2014 036 02/05 16:05 occurs at a notably low latitude, as it can be seen in Fig. 3.11. Furthermore, in Fig. 3.8 the approximated CME's direction of propagation is indicated. With a spacecraft separation of around 50^{o} and taking into account that the CME is clearly moving towards STEREO Ahead, it can be inferred that this event is not a good candidate for multipoint observations, as it would need to be extremely wide in order to touch the other twin spacecraft.

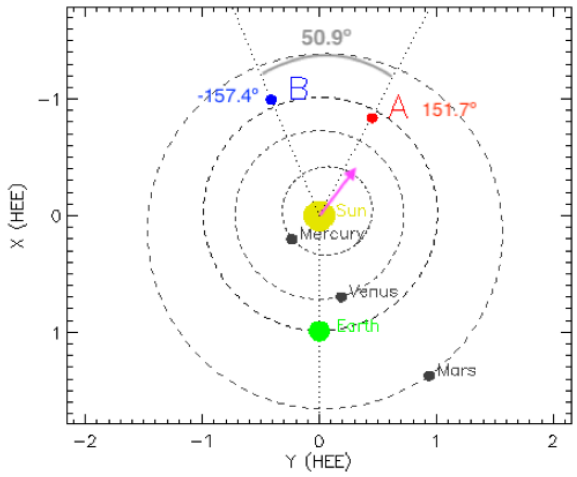

Figure 3.8: Simplified depiction of the relative position between the STEREO spacecraft and the ICME being ejected in February, 2014 (DOY 036).

3. **Event 3: April 2014**
   Finally, the event detected by STA on the 2014 101 04/11 15:24 and STB on the 2014 102 04/12 02:27 shows that the CME is appears for the first time almost on the Sun's equator (Figure 3.12) and is clearly being ejected towards STEREO Behind. This and the fact that the event seems to be relatively faint, would make it very difficult to analyze the shape and geometrical parameters of the structure from the images in future steps of the study. This is why the event is no longer considered a good candidate for the continuation of this work.

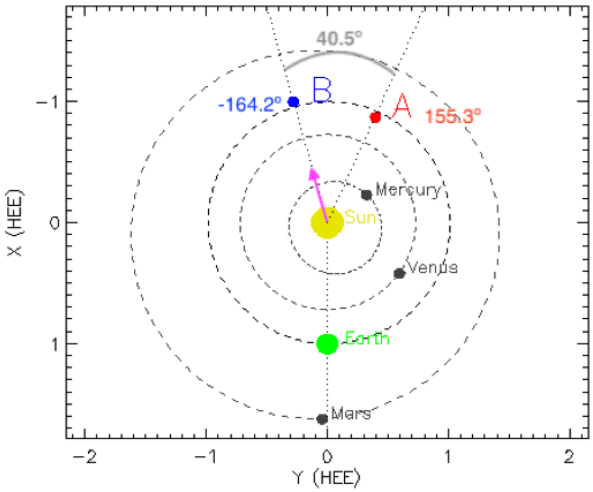

Figure 3.9: Simplified depiction of the relative position between the STEREO spacecraft and the ICME being ejected in April, 2014 (DOY 101).

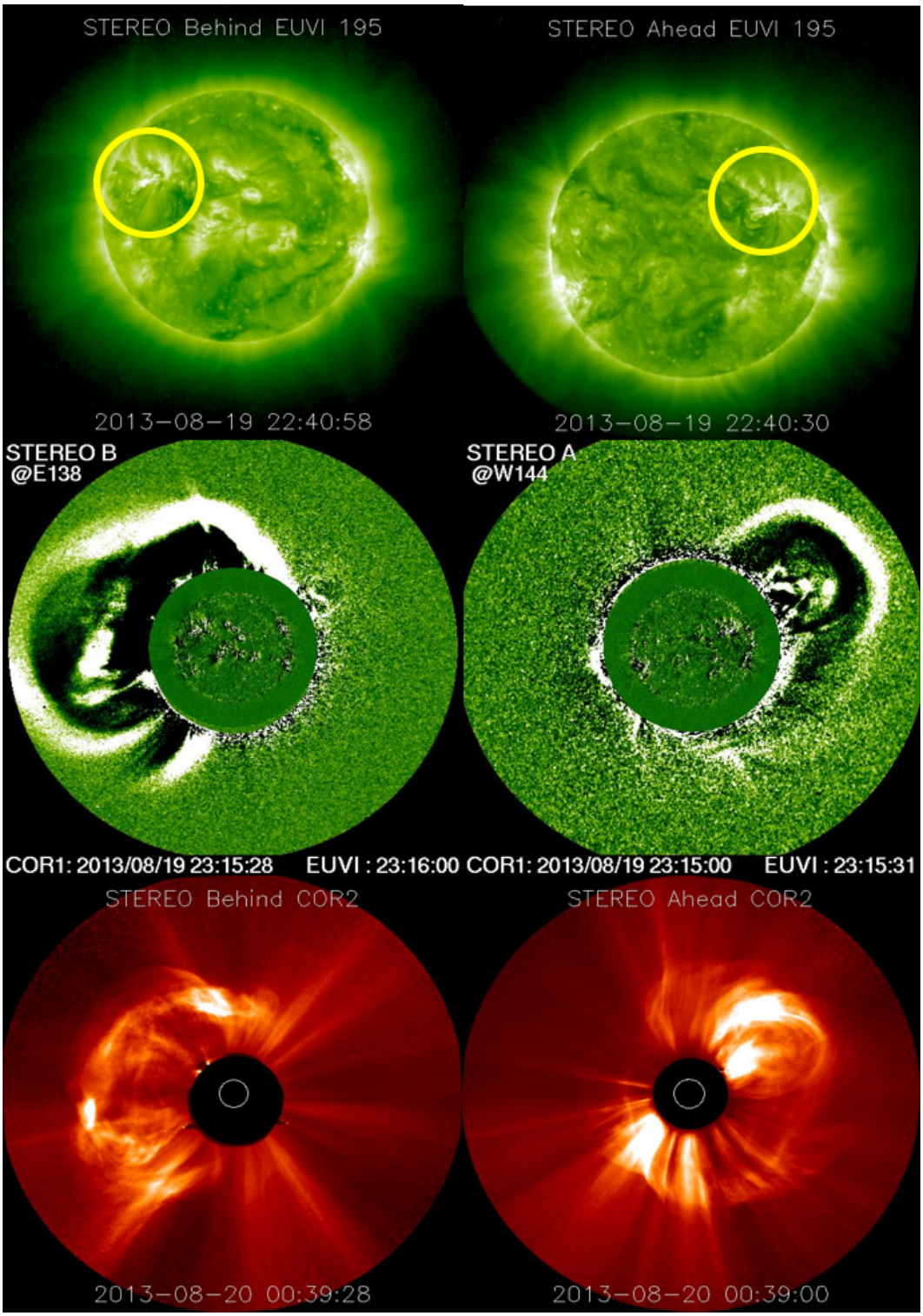

Figure 3.10: *Top row*: a CME erupting from an active region on 2013-08-19T22:40:30. *Middle/Bottom row*: the evolution of such CME observed with COR1RD and COR2, respectively. The left column corresponds to the images taken by STB and the right column to STA's.

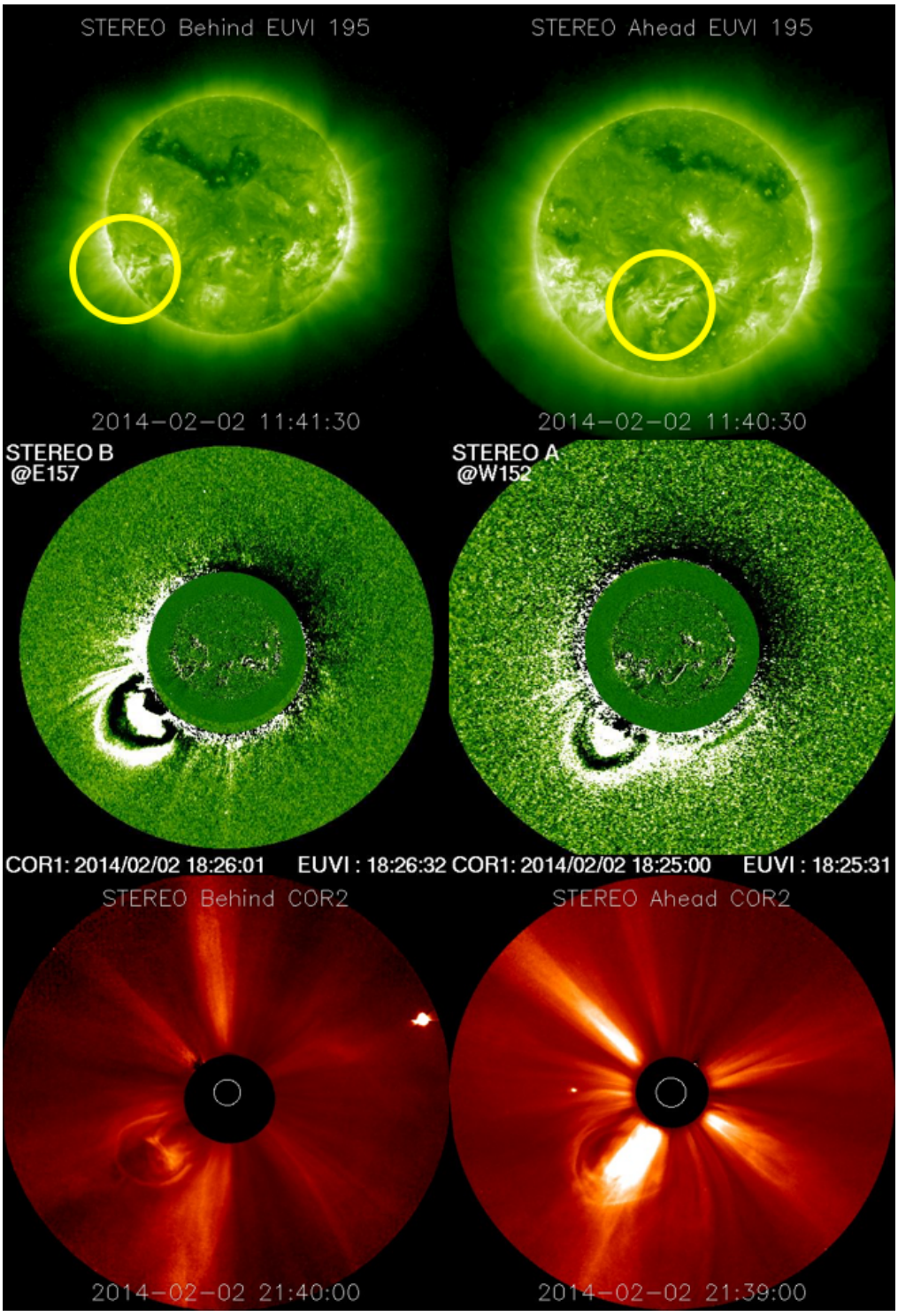

Figure 3.11: *Top row*: a CME erupting from an active region on 2014-02-02T11:40:30. *Middle/Bottom row*: the evolution of such CME observed with COR1RD and COR2, respectively. The left column corresponds to the images taken by STB and the right column to STA's.

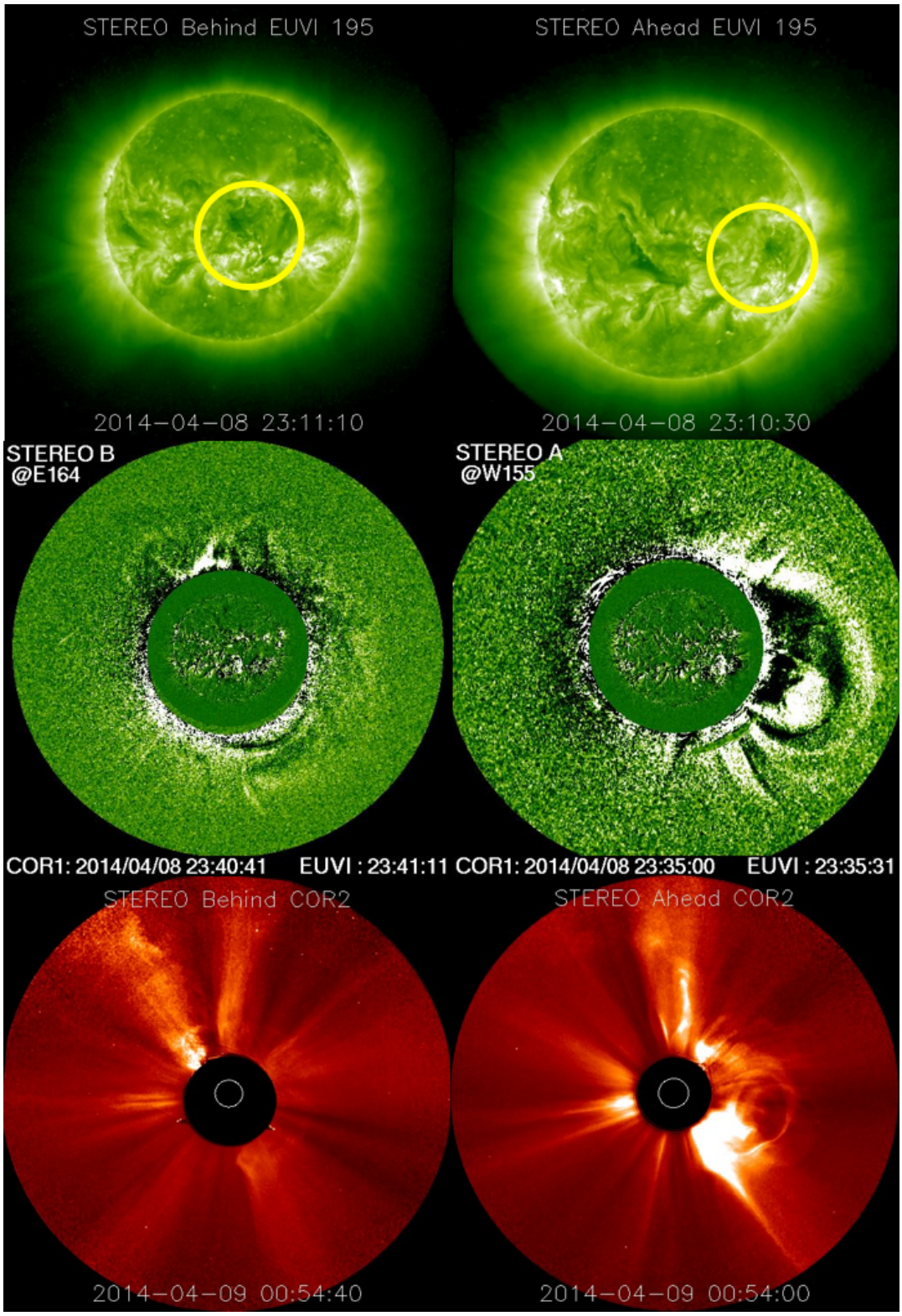

Figure 3.12: *Top row*: a CME erupting from an active region on 2014-04-08T23:10:30. *Middle/Bottom row*: the evolution of such CME observed with COR1RD and COR2, respectively. The left column corresponds to the images taken by STB and the right column to STA's.

3.2.3 Selection of the final candidate

The results derived from the categorization of events, remote sensing analysis and final filtering presented in the previous sections yield to the consideration of **Event 1: 2013 234 08/22 07:05 STA and 2013 170 06/19 15:08 STB** as the final candidate. Thus, from now on, the analysis and discussions presented in this work will be based solely on this event, due to its high interest for the purpose of linking the in-situ measurements, analytical models and imaging techniques that now will be developed.

4 | Comprehensive analysis of the final candidate

4.1 In-situ measurements results and analysis

After filtering all the different events between 2013 and 2014 and performing the selection of the final one for the purpose of this work, a first comprehensive analysis of the in-situ signatures corresponding to its ICME structure is presented in this section. The radial distance to the sun, longitude and latitude in HEE coordinate system for STEREO A, B and MESSENGER at the Magnetic Obstacle's start time for each case is presented in Table 4.1.

Figure 4.1a displays the magnetic field and proton plasma observations by STEREO A. The ICME extends from 07:05 UT on August 22, 2013 (234, vertical black line) to 23:25 UT on August 24 (236, second dashed line). The ICME period is marked with a horizontal black line at the top of the figure. The magnetic obstacle, marked with a horizontal pink line at the top of the figure, is bounded by the two dashed lines (from 23:15 UT on August 22 to 23:25 UT on August 24) with an increase of the magnetic field strength (top panel) and two partial rotations of the B_N component (second panel from the top). The fourth panel from the top shows the depression in the proton plasma thermal speed in the same interval as the depression in the β_p. At the bottom, Figure 4.1b displays the combined magnetic hodograms of pairs of RTN magnetic field components. Overplotted with a pink line is the hourly data average and the start time is marked with a red dot. Following the pink line, the magnetic complex configuration is confirmed by the aforementioned partial rotations of the magnetic field vector in the $N-T$ plane (see $B_N - B_T$ hodogram): a first northward rotation, followed by a southward rotation after a change in the parameters' behavior that is observed at around DOY 236.

	MO Start Time	**Long [°]**	**Lat [°]**	R_{Sun} [AU]
STEREO A	2013-08-22T23:17:00	144.7	-0.1	0.9673
STEREO B	2013-08-22T12:57:00	-138.0	-0.2	1.0252
MESSENGER	2013-08-20T19:12:00	162.7	6.9	0.3299

Table 4.1: For each of the spacecraft STEREO A, B and MESSENGER: 1) Magnetic Obstacle start time, 2) longitude in HEEQ, 3) latitude in HEEQ and 4) distance to the Sun at the time of detection.

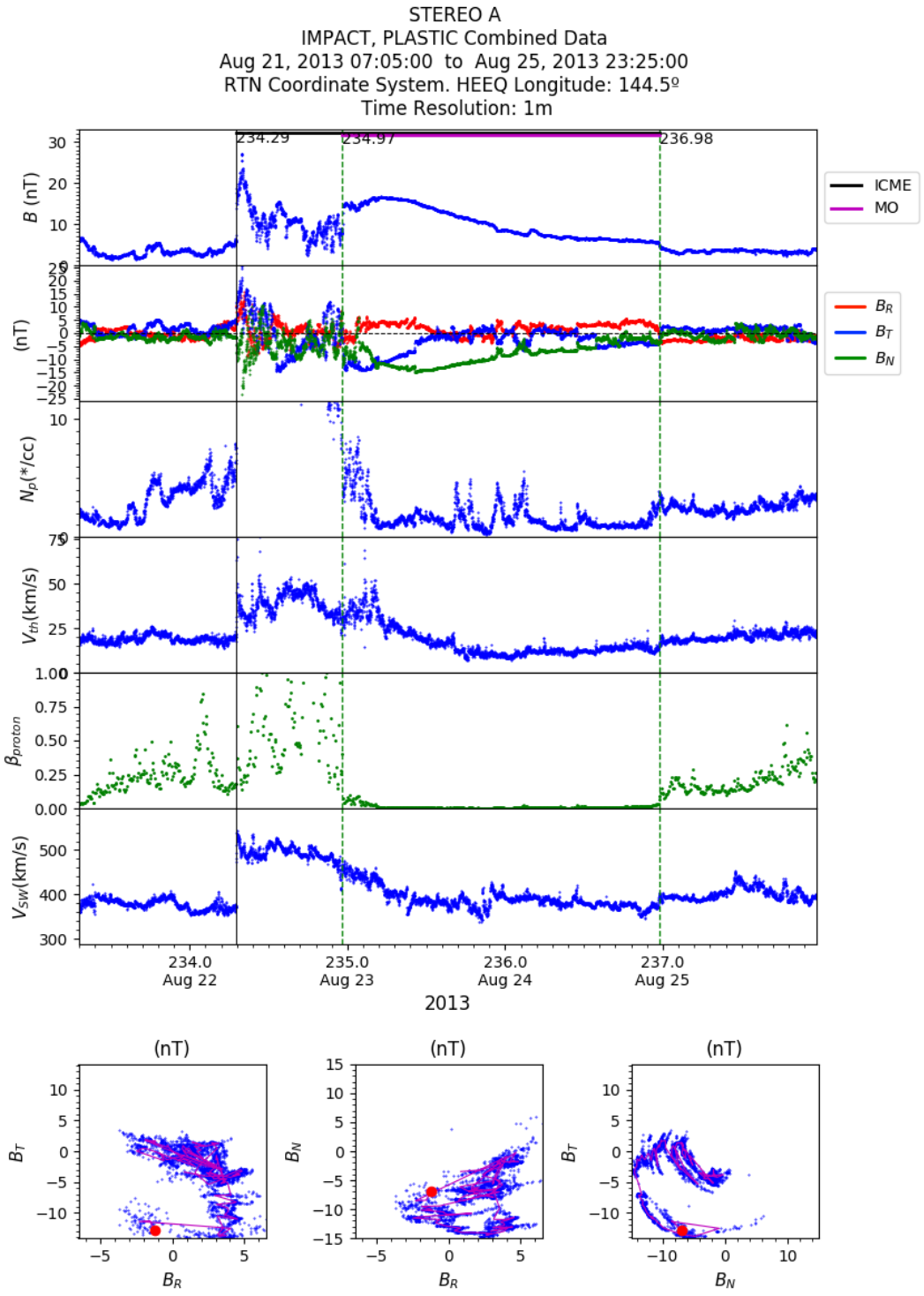

Figure 4.1: a) In situ data from the IMPACT and PLASTIC instruments onboard the STEREO A spacecraft on August 21-25, 2013.

In the case of STEREO B (see Figure 4.3a, the ICME and the MO extend from 02:10 UT on August 22, 2013 (234, vertical black line) to 07:00 UT on August 23 (236, second dashed line) and from 13:00 UT on August 22 to 07:00 UT on August 23, respectively. In juxtaposition to STEREO A's results, these parameters

do not show clear signatures, as no behavioral patterns that govern the nature of the magnetic field rotation (see Figure 4.3b are observed, the structure is notably disordered and, in the end, no ordered topology or monotonic change in the magnetic field is detected. Thus, following the criteria presented in Section 3.1, these signatures correspond to an ejecta type of configuration and could be a sign, a priori, that the spacecraft is crossing one of the legs of the structure or just detecting the IPS(interplanetary shock) without necessarily cutting across the ICME.

Finally, Figure 4.2a displays the magnetic field measurements provided by MESSENGER. The ICME extends from 12:18 UT on August 20, 2013 to 08:38 UT on August 21. The MO starts at 17:49 UT on August 20, 2013 and its end matches the end of the ICME. In this case, it is possible to observe two partial rotations of the B_N component (see magnetic hodograms), as it occured with STA as well. Each of these rotations has been highlighted in a different color (purple and green) on the plot.

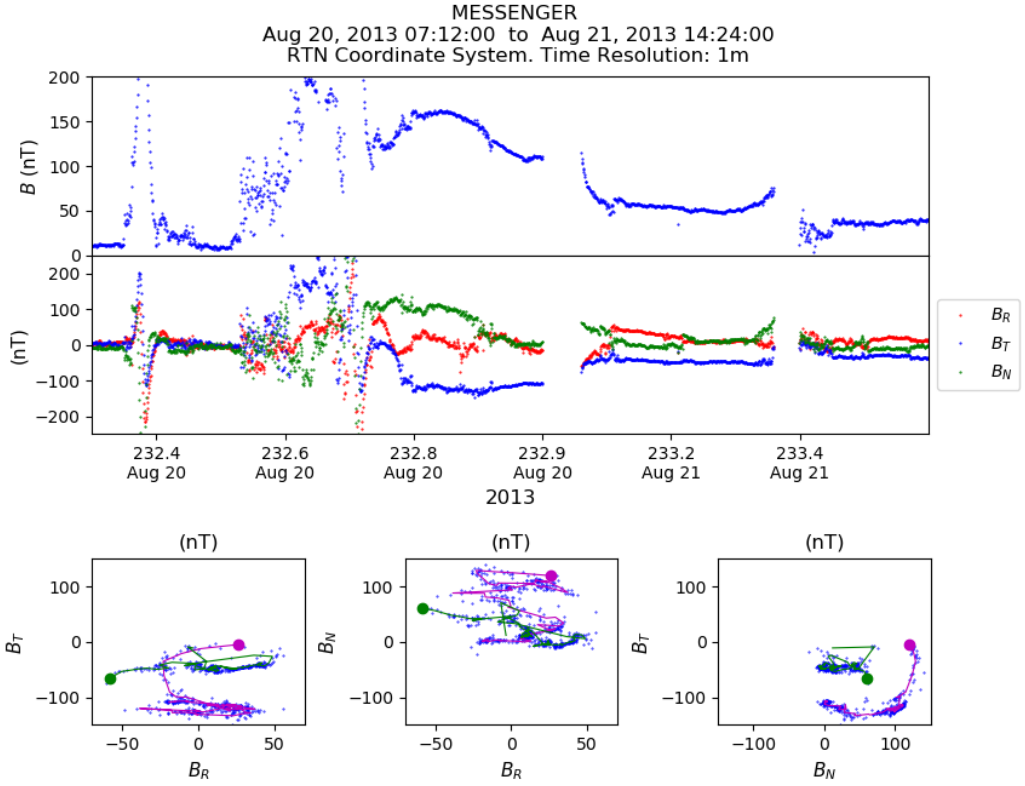

Figure 4.2: a) In situ data from the MAG instrument onboard the MESSENGER spacecraft on August, 2013. From the top, the magnetic field magnitude and components in the RTN coordinate system. (b) Three combined magnetic hodograms in RTN coordinate system.

Taking into account that, according to Figure 4.11, STEREO A and MESSENGER seem to be crossing similar sections corresponding to the front of the same ICME, a comparison between the measurements obtained for the B_N component that each of the spacecrafts detect (see Figure 4.1 and 4.2) yields to very interesting results. In this way, it is easy to observe that the profiles of $B_N^{MESSENGER}$ and $B_N^{STEREO\,A}$ are very similar in shape, but have different signs, which is something quite unsual for this case considering the position of the spacecraft. A close-up view of this

phenomenon can be seen in Figure 4.4.

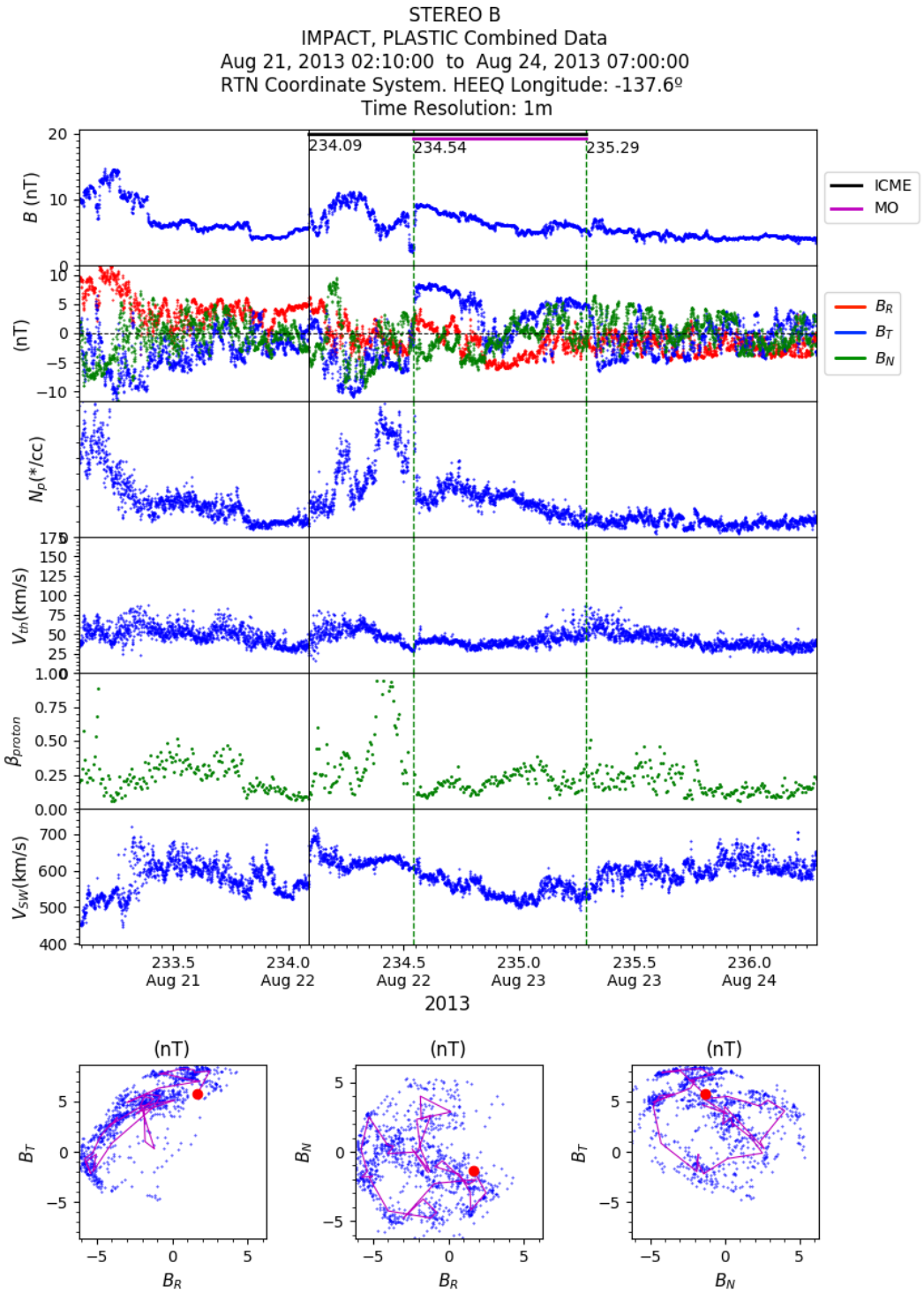

Figure 4.3: a) In situ data from the IMPACT and PLASTIC instruments onboard the STEREO B spacecraft on August 21-24, 2013.

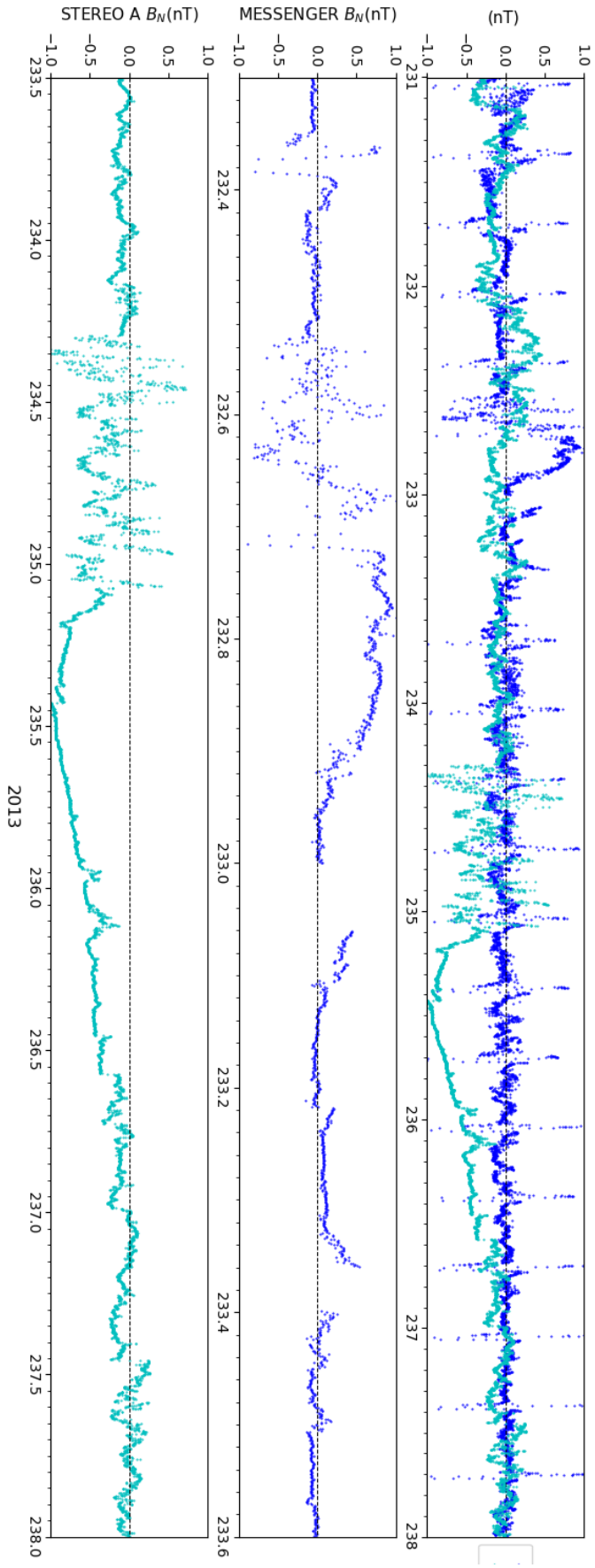

Figure 4.4: Comparison between the in-situ observations provided by STEREO A and MESSENGER.

4.2 Forward modelling of the ICME

Now that the final event for the study have been selected, a three-dimensional reconstruction of the ICME will be presented in order to check the obtained results and further proceed with the study. The 3D reconstruction of the event will be performed by means of the Graduated Cylindrical Shell Model [20], an innovative model developed by A. Thernisien that is being widely use among the Space Weather scientific community.

In order to work with this model, the Solarsoft environment must be utilized. Solarsoft is a collaborative software development system created at Lockheed-Martin to support solar data analysis and spacecraft operation activities. It is widely recognized in the solar physics community as having revolutionized solar data analysis starting in the early 1990s. Solarsoft is in active development and use by research groups on all seven continents.

4.2.1 Graduated Cylindrical Shell (GCS) model description

The graduated cylindrical shell (GCS) model ([20]) has been used with the goal of studying the three-dimensional morphology, position, and kinematics of coronal mass ejections observed by coronagraphs. The model is built using the following features and constraints: (1) the legs of the structure are conical, (2) the front is pseudo-circular, (3) the cross section is circular, (4) it expands in a self-similar way.

The graduated cylindrical shell (GCS) is an empirical model to represent the flux rope structure of some coronal mass ejections (CMEs). After decades of CME observations and classification based on their morphological similarities ([5]), the flux rope morphology is emerging as the most typical three-dimensional shape we can use to represent CMEs. Another important property of CMEs is that they tend to expand self-similarly. The GCS model is developed to integrate both the self-similar expansion and the flux rope three-dimensional morphology.

The model can be used to obtain estimations of parameters such as CME position, direction, three-dimensional extent, true speed, and even, but with a smaller confidence, its orientation. Since its introduction, the GCS has been employed in many other studies. For example, [16] determined the kinematics and expansion speed of four events from 5 R_{Sun} to 80 R_{Sun} using the STEREO/SECCHI COR2 and Heliospheric Imager instrument fields of view. [10] compared the GCS modeling of two CME events with flux rope reconstruction using in situ measurements at 1 AU.

The GCS is often called the *hollow croissant* because of its shape. Figure 4.5 gives the schematic of the model: the left panel shows a planar cut of the croissant viewed face-on, while the right panel shows a planar cut of the same croissant viewed edge-on. The two legs are conical and the front is reminiscent of a torus with its cross-section radius increasing with height.

The parameters of the model are the following:

As in [21] and [20] κ ($\kappa = \sin\delta$) acts as the *aspect ratio* of the model. This parameter sets the rate of expansion versus the height of the CME, so the structure expands

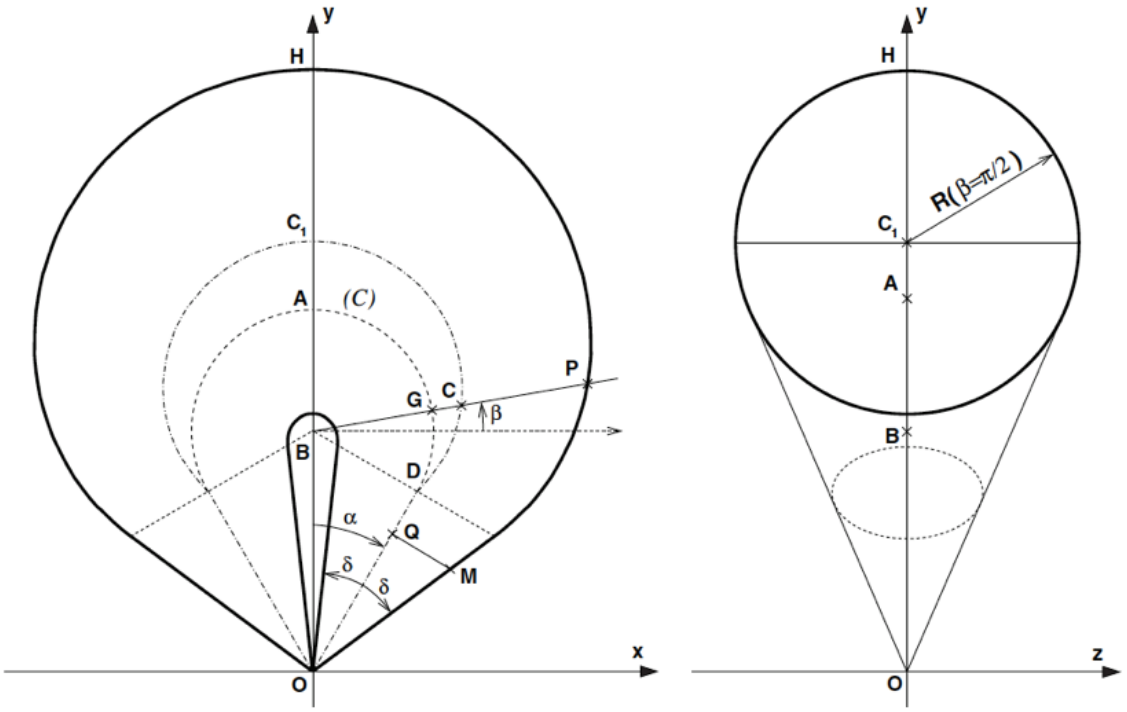

Figure 4.5: Schematic of the GCS model. The left panel shows a $(O, \mathbf{x}, \mathbf{y})$ planar cut of the croissant viewed face-on. The z-axis points toward the reader. The right panel shows a cut in the $(O, \mathbf{y}, \mathbf{z})$ plane where the croissant is viewed edge-on. In this view, only the circle (solid line) is in the $(O, \mathbf{y}, \mathbf{z})$ plane. Figure from [19].

in a self-similar way. The second parameter is the *full height* of the cone, which is the distance OD: OD $= h$. The third and last parameter, α, is the angle between the axis of the leg and the y-axis: the *half-angle*. The three parameters κ, h, and α suffice to fully define the geometry of the model.

The important aspects of the geometry are summarized here:

1. The GCS is constrained to expand in a self-similar way.

2. The front part is not circular, though it has been built using a circular generating line.

3. The cross section of the front part is a circle in the planes $(B, \vec{BG}, z)$.

4. The front of the GCS becomes spherical when the half-angle parameter is zero. In that case, it is equivalent to a hollow ice-cream cone.

Figure 4.6 shows how the GCS model is located in 3D space with respect to the solar surface. Most of the position parameters are taken from the observations of the neutral line of the SR for the CME being modeled. The model is positioned normal to the photosphere with the legs at the opposite ends of the neutral line. The neutral line is centered at a given Carrington longitude (ϕ) and latitude (θ) with a tilt (γ) relative to the solar equator.

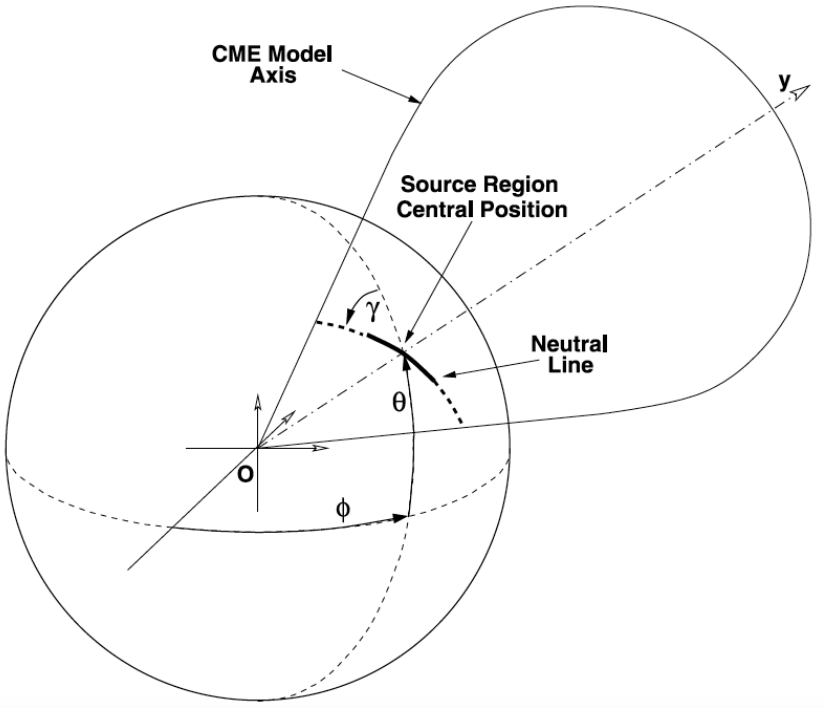

Figure 4.6: Location of the GCS model in 3D space based on observations of the SR neutral line. Original figure from [21].

4.2.2 GCS implementation and results

In order to derive the three-dimensional morphology and orientation of the CME flux rope, the Graduated Cylindrical Shell [20] forward-fitting model to simultaneous observations from three vantage points (SECCHI A, B and LASCO) has been applied. As it has been explained in Section 4.2.1, this model allows to study the shape, position and kinematics of CMEs by generating a three-dimensional representation of an idealized flux rope. It is necessary to highlight that the fit corresponds to the flux rope (cavity) and not the leading edge of the structure, as the latter is due to material pileup in front of the flux rope (the so-called sheath). In this case, COR1 and COR2 images were used at lower and higher distances, respectively, to help track the propagation and evolution of the ICME in a more precise way.

Table 4.2 shows the resulting parameters corresponding to the three different instant times at which the reconstruction was conducted: 1) *Long:* longitude [°] in Carrington system; 2) *Lat:* latitude [°]; 3) *Rot:* tilt angle [°]; 4) *Hei:* height [R_{Sun}]; 5) *Ratio:* aspect ratio, which sets the rate of expansion versus the height of the CME; 6) *Half:* half angle [°], or the angle between the axis of the leg and the y-axis. These parameters correspond to the 3D reconstruction images of STEREO A, B and LASCO that can be observed in Figure 4.7. Taking into account the aforementioned fitting, parameters and spatial location of the spacecraft, it can easily be inferred that the structure is clearly heading towards STA and MESSENGER, and probably too tilted to cross STB.

In order to derive the parameters shown in Table 4.2, first, the two-dimensional images corresponding to the COR2 photos taken by STEREO for all the different instants in which GCS model will be applied are download by means of the SolarSoft environment. These images have been enclosed in Figure 4.8. From them, it is possible to infer the spatial 2D boundaries of the CME and its time evolution so that, manually, the GCS 3D green wireframe can be adjusted to the shape of the images for each time being considered. As the aim of this model is to recreate the 3D ICME structure from the 2D available images, the more viewpoints the better and more precise results. That is the reason why the LASCO observatory has also been added to the analysis for the generation of the fitting.

Date	**Time**	**Long**	**Lat**	**Rot**	**Hei**	**Ratio**	**Half**
2013-08-19	23:25	327.578	8.383	34.659	5.50	0.4000	59.814
2013-08-19	23:54	326.459	0.000	33.539	8.00	0.4251	59.814
2013-08-20	00:24	326.459	0.000	36.335	11.57	0.4251	59.255
2013-08-20	00:54	326.459	-5.031	36.335	15.36	0.4251	59.255
2013-08-20	01:24	326.459	-5.031	39.690	17.50	0.4251	59.534
2013-08-20	01:54	326.459	-5.031	36.335	20.64	0.4251	59.255

Table 4.2: Obtained value for each of the GCS model parameters for each time in which the reconstruction technique has been applied for the event of study.

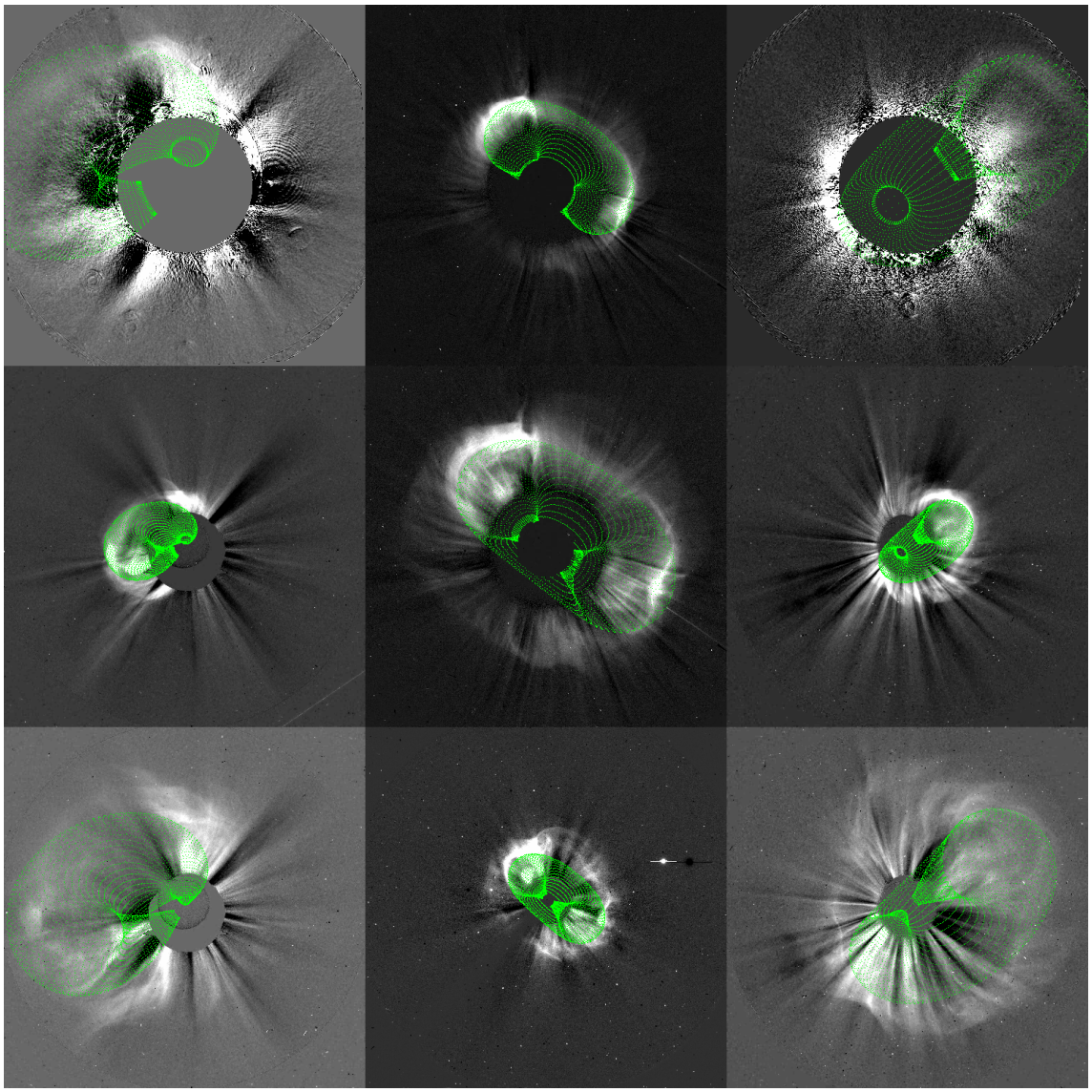

Figure 4.7: A sequence of nine STEREO and SOHO/LASCO images of the ICME, each row corresponding to a different time instant: 2013-08-19T23:25:00, 2013-08-19T23:54:00 and 2013-08-20T01:24:00, in chronological order, with the related 3D reconstruction by means of the Graduated Cylindrical Shell (GCS) model. Top panel: COR1-B (left), LASCO-C2 (middle), COR1-A (right). Middle panel: COR2-B (left), LASCO-C2 (middle), COR2-A (right). Bottom panel: COR2-B (left), LASCO-C3 (middle), COR2-A (right).

From the obtained parameters, several conclusions can be drawn: first, the ICME certainly verifies the hypothesis of *self-similar expansion*, as the aspect ratio remains almost constant at all instants. Furthermore, the structure experiments a slight rotation from the moment it is ejected to later times, as the latitude angle changes from 8.383°at 23:25h to -5.031 at 00:54. However, it finally becomes stable, as no major modifications in its value occur from this time to 01:54. Finally, the longitud, tilt and half angle, all show almost constant values. Thus, from these results, a first assuption that the ICME presents a smooth behaviour with minor variations in its rotation angles will be made.

Figure 4.8: A sequence of ten COR2 STEREO A and B 2D images of the ICME, each row corresponding to a different time instant: 2013-08-19T23:54:00, 2013-08-20T00:24:00, 2013-08-20T00:54:00, 2013-08-20T01:24:00 and 2013-08-20T01:54:00. The left column corresponds to the observations made by STB and the right column is related to STA.

4.3 Flux-rope topology from in-situ measurements

For more than 30 years, scientists have been working on understanding the geometry and the physical characteristics of the heliospheric magnetic structures known as Magnetic Clouds ([2]) entrained within interplanetary coronal mass ejections (ICMEs). By definition, MCs show an increase in the magnetic field strength, with a monotonic magnetic field rotation (flux-rope) resulting in large net rotation of at least one of the magnetic field components. The plasma parameters show a low proton plasma temperature and plasma-β_{proton} (ratio of the plasma to magnetic pressure) below 1. In the best examples, the in situ magnetic flux-rope signatures are consistent and simultaneous with the plasma parameters behavior in the MC defined structure. In general, the circular-cylindrical linear force-free model/technique ([9]) has been, and continues to be, the standard model for describing the magnetic field observations in these cases.

Generally, however, the observed magnetic field signatures are more complex than a simple flux-rope magnetic topology. Those events are classified as MC-like (MCL) or Ejecta ([8]). Imaging observations of CMEs close to the Sun also provide evidence for the existence of flux-rope structures within CMEs ([18],[22]) but observations out in the heliosphere also suggest that the CME, and presumably the entrained flux-rope, undergo significant evolutionary changes, such as deformation or distortion, during their heliospheric propagation ([12]).

Taking all the aforementioned information into account, the most recent optimizations of the *Circular-cylindrical Analytical Flux Rope Model for Magnetic Clouds* and the *Elliptic-cylindrical Analytical Flux Rope Model for Magnetic Clouds* developed by Teresa Nieves Chinchilla et al. have been chosen for the analytical study of the particular event presented in this work, as these models contemplate many different scenarios and provide quite general results with high accuracy that are very appropriate for the aim of this work.

4.3.1 Circular-cylindrical Analytical Flux-rope Model for Magnetic Clouds (CCAMMC) description

This model is a generalization of the circular-cylindrical case originally published by [3]. The model considers the MC as a flux-rope but without discarding the role of the plasma pressure, which can be significant at some distance to the Sun or play a role in the physical processes of the interaction with the solar wind. The magnetic flux-rope topology is obtained from Maxwell's equations on a circular-cylindrical coordinate system, and under steady-state conditions. The model does not impose a force-free condition and solely establishes profiles for the current density components.

The model uses the circular-cylindrical coordinate system (Figure 4.9):

$$x = r\cos\varphi,\ y = y,\ z = r\sin\varphi \tag{4.1}$$

The base vectors are:

$$\begin{aligned} \epsilon_r &= \cos\varphi\, u_x + \sin\varphi\, u_z \\ \epsilon_y &= u_y \\ \epsilon_\varphi &= -r\, \sin\varphi\, u_x + r\, \cos\varphi\, u_z \end{aligned} \tag{4.2}$$

In this coordinate system, the Maxwell equations, $\Delta \cdot B = 0$, $\Delta \times B = \mu_0 j$ and $\Delta \cdot j = 0$ can be solved under the *cylindrical approximation*: without the radial magnetic field component, $B_r = 0$, and with axial invariance. Moreover, although any of the current density components can be non-zero in the most general case, the radial current is not taken into account for simplicity in this case ($j_r = 0$), so that $j_\varphi = j_\varphi(r)$ and $j_y = j_y(r)$. Then, the magnetic field components are given by

$$\begin{aligned} B_r &= 0 \\ B_y &= B_y^0 + \mu_0 \int_0^r j_\varphi(r')\mathrm{d}r \\ B_\varphi &= -\frac{\mu_0}{r} \int_0^r r' j_y(r')\mathrm{d}r' \end{aligned} \tag{4.3}$$

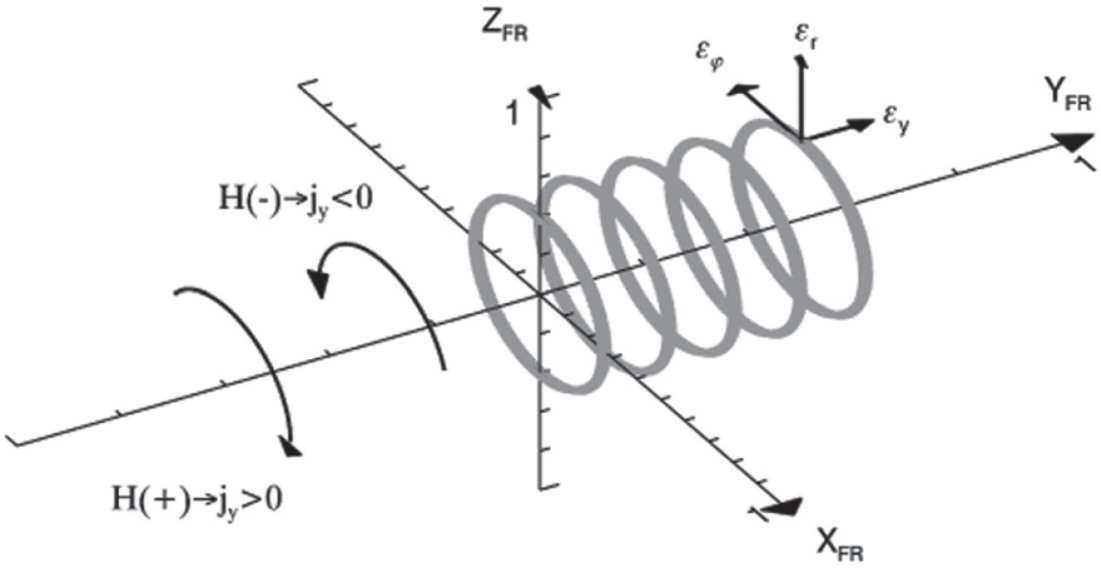

Figure 4.9: Cylindrical-circular unit base vectors for a flux-rope along the y-axis. The *handedness* is also indicated according to the axial current component sign under the assumption that $By \geq 0$. Figure from [13].

By convention, it is assumed that the component B_y is positive and increases from a minimum at $r = R$ toward a maximum at the axis. Equations (4.3) describe the core of this model and any other physical quantity such as, for instance, the axial (ϕ_y) and poloidal (ϕ_φ) magnetic fluxes, can be derived from these equations. Also, *handeness* or *chirality* (H in Figure 4.9) is defined by the sign of j_y (axial current density component) because j_φ is assumed to be negative. Finally, the number of turns in the flux-rope per axial length is determined by the model components as:

$$N_L(r) = \left| \frac{B_\varphi}{2\pi r B_y} L \right| \tag{4.4}$$

In order to perform the computational implementation of the model in an efficient way and shape the current density radial variations, all the different parameters are expressed as polynomial functions, with α_n and β_m arbitraty coefficients to be determined and B_y^0 a boundary condition for the flux-rope.

$$\begin{aligned} B_r &= 0 \\ B_y &= B_y^0 - \mu_0 \sum_{n=1}^{\infty} \alpha_n \frac{1}{n+1} r^{n+1} \\ B_\varphi &= -\mu_0 \sum_{m=0}^{\infty} \beta_m \frac{r^{m+1}}{m+2} \\ j &= \sum_{m=0}^{\infty} \beta_m r^m e_y - \sum_{n=1}^{\infty} \alpha_n r^n e_\varphi \end{aligned} \tag{4.5}$$

Also, to avoid singularities in the axis, the following constraints can be applied: $m = [0, \infty)$ and $n = [1, \infty)$. For futher details on the analytical development of the model, see [13].

The part of the model that is the most interesting for the purpose of this work is, however, the *reconstruction technique* that it offers, which is based on a multiple regression method to infer the spacecraft trajectory (r_{sat}, $\sin\varphi_{sat}$) within the ICME to minimize the X^2 using a *Levenberg-Marquardt* algorithm ([17]). This is achieved by means of an iterative exercise: going from the local flux-rope coordinate system to the spacecraft coordinate system as follows,

$$\begin{aligned} B_x^{GSE} &= B_x^{local}\cos\phi - B_y^{local}\sin\phi\cos\theta + B_z^{local}\sin\phi\sin\theta \\ B_y^{GSE} &= B_x^{local}\sin\phi + B_y^{local}\cos\phi\cos\theta - B_z^{local}\cos\phi\sin\theta \\ B_z^{GSE} &= B_y^{local}\sin\theta + B_z^{local}\cos\theta \end{aligned} \tag{4.6}$$

where ϕ and θ are the longitud and tilt angle of the flux-rope in GSE coordinate system, respectively.

A single term from the polynomial functions presented in Equations (4.5) will be taken into account for simplicity. Hence, the model is finally reduced to,

$$\begin{aligned} B_r &= 0 \\ B_y &= \mu_0 \frac{\alpha}{2}\left(\tau R^2 - r_{sat}^2\right) \\ B_\varphi &= -\mu_0 j_y \frac{r_{sat}}{2} \\ j_y &= \beta_0 \,(m=0) \\ j_\varphi &= \alpha r \,(n=1) \end{aligned} \tag{4.7}$$

Now, there are two main steps for the reconstruction:

1. **Initial/guess parameters**: α^g,j_y^g,ϕ_{MVA}, θ_{MVA}.
   There are two types of parameters: geometrical -related to the shape and orientation of the ICME- and physical -related to the current density components (j_y,α)-. Assuming that the cross-section size (R_{approx}) can be approximated as

the MO time interval times the mean solar wind bulk velocity inside the MO, then the guess parameters are obtained from Equations (4.7), with B_{mean} and B_{min} the mean and minimum value of the magnetic field strength observed in the MO time period ($B_{min} \sim B_\varphi(r = R)$ and $B_{mean} \sim B_y(r = 0)$, respectively):

$$\begin{aligned} \alpha^g &= \frac{|B_{mean}|}{\mu_0 R_{approx}^2} \\ j_y^g &= \pm \frac{|B_{min}|}{\mu_0 R_{approx}} \end{aligned} \tag{4.8}$$

Therefore, these two parameters plus the angles obtained from *minimum variance* (ϕ_{MVA} and θ_{MVA}), which is a method used to extrapolate the priviledge direction for the flux-rope, constitute the set of *guess* parameters for the next step in the reconstruction. Finally, α is imposed to be always positive to ensure a positive direction for the axial component of the magnetic field by convention.

2. **Fitting procedure**.
   The fitting procedure is built to achieve a minimum in the chi-squared residue ([17]) as described on [3]. From the initial (guess) parameters, the iterative procedure yields the best-fit set of parameters. Sometimes manual adjustments are needed to help the routine converge to the best solution. From this fitting algorithm it is possible to infer the spacecraft trajectory through the structure. The satellite local-cylindrical coordinates along the MC are

$$\begin{aligned} r_{sat} &= \sqrt{x_{sat}^2 + z_{sat}^2} \\ \sin\varphi_{sat} &= \frac{z_{sat}}{r_{sat}} \end{aligned} \tag{4.9}$$

   where x_{sat} and z_{sat} are local-cartesian flux-rope coordinates obtained from the observations:

$$\begin{aligned} x_{sat} &= (v_{sw}t - x_0)\cos\phi \\ z_{sat} &= \sin\phi \sin\theta\,(v_{sw}t - x_0) - Z_0\cos\theta \end{aligned} \tag{4.10}$$

   The x_0 value is obtained under the condition that the flux-rope cross-section is constant between the spacecraft entrance and exit, and Z_0 provides the information needed to find the spacecraft's closest distance to the flux-rope axis (Y_0) (Equation (3) on [4]).

Finally, the goodness of the fit can be evaluated by means of the *correlation coefficient*, ρ, which is defined as

$$\rho = \frac{\rho_t + \rho_x + \rho_y + \rho_z}{4} \tag{4.11}$$

where ρ_i is the correlation coefficient for each normalized magnetic field dataset included in the fitting procedure. For cataloguing purposes, the success of the reconstructions is split into three ranges:

1. Very good: $\rho \geq 0.7$
2. Good: $0.5 \leq \rho \leq 0.7$
3. Poor: $\rho \leq 0.5$

4.3.2 Elliptic-cylindrical Analytical Flux-rope Model for Magnetic Clouds (ECAMMC) description

This model adds complexity to the geometry described by the CC by allowing an elliptic cross section for the cylinder. This approximation describes the magnetic flux rope topology with a distorted cross section as a possible consequence of the flux rope interaction with the solar wind. The mathematical formulation of the model is very similar to the previous case, but taking into account that the section of the structure is now elliptical (thus, it has not been included in this report). Further details on the analytical development of the equations that serve as the base for the model, can be consulted in [14].

Along the same lines as in the previous section, the local Cartesian components of the magnetic field are transformed in the spacecraft coordinate system, Geocentric Solar Ecliptic (GSE), so that

$$B^{GSE} = AB_{Local} = Y_3(\xi)X_2(\theta)Z_1(\phi)B_{Local} \tag{4.12}$$

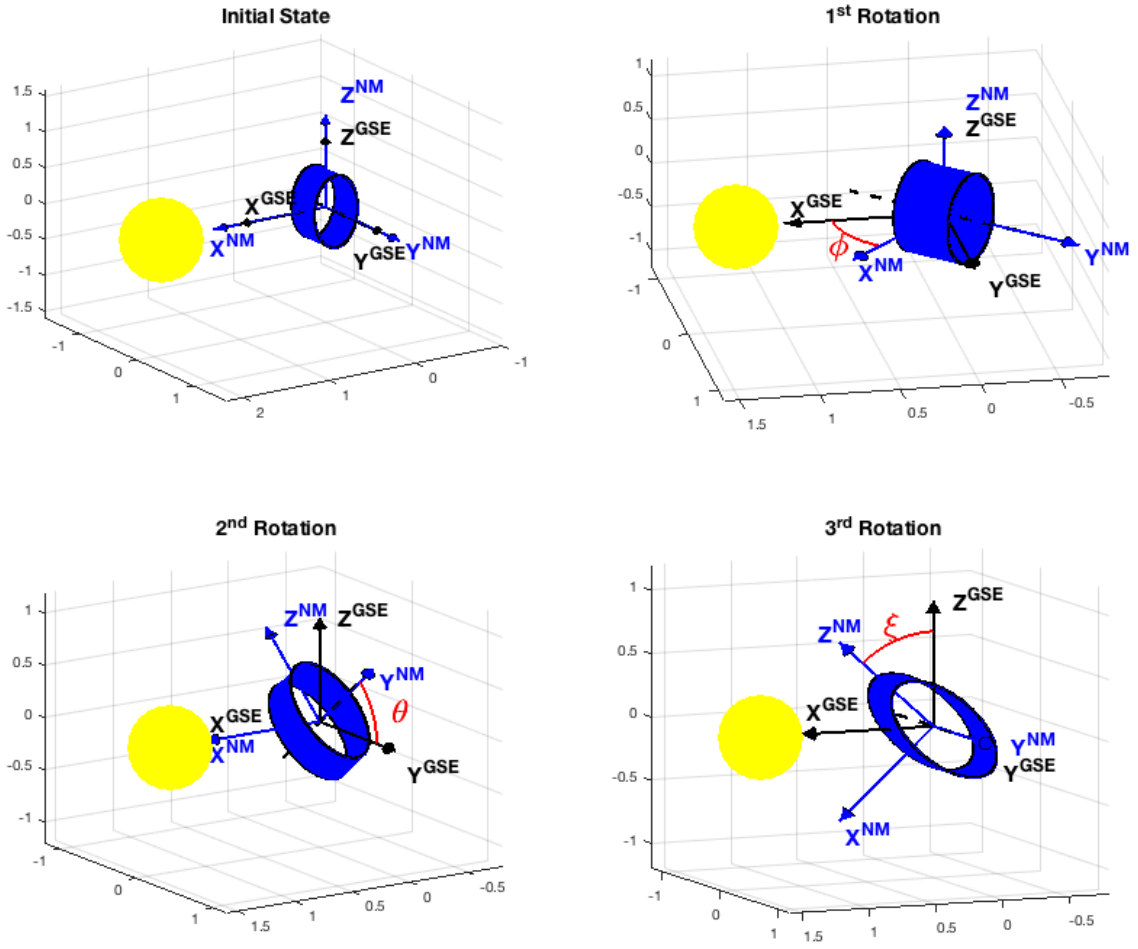

Figure 4.10: Illustration of the three orientation angles: the longitude (ϕ), the tilt (θ) and the *propagation angle* (ξ). In the figures, X^{NM}, Y^{NM}, Z^{NM} correspond to the local cartesian coordinate system and $X^{GSE}, Y^{GSE}, Z^{GSE}$ to the spacecraft coordinate system.

Thus, the rotation matrix A defines the rotations that occur about the axis of the local coordinate system (NM) attached to the modeled flux-rope following the order

yaw-roll-pitch; where the angles ϕ (longitude), θ (tilt) and ξ (angle of propagation), correspond to the first, second and third rotation about the intrinsic axis of the structure. The final shape of matrix A is enclosed in Equation (4.13).

$$A = \begin{bmatrix} \cos\phi\cos\xi - \sin\phi\sin\theta\sin\xi & -\sin\phi\cos\theta & \cos\phi\sin\xi + \sin\phi\sin\theta\cos\xi \\ \sin\phi\cos\xi + \cos\phi\sin\theta\sin\xi & \cos\phi\cos\theta & \sin\phi\sin\xi - \cos\phi\sin\theta\cos\xi \\ -\cos\theta\sin\xi & \sin\theta & \cos\theta\cos\xi \end{bmatrix} \tag{4.13}$$

The spacecraft trajectory within the structure is defined by (x_{sat}, 0, $-z_0$) in the GSE coordinate system. Thus, in the local Cartesian coordinate system, (x_L, y_L, z_L):

$$\begin{aligned} x_L &= (\cos\phi - \sin\phi\sin\theta\sin\xi)\, x_{sat} + z_0\cos\theta\sin\xi \\ y_L &= -\sin\phi\cos\theta x_{sat} + z_0\sin\theta \\ z_L &= (\cos\phi + \sin\phi\sin\theta\cos\xi)\, x_{sat} - z_0\cos\theta\cos\xi \end{aligned} \tag{4.14}$$

In order to better understand how these rotations work, an easy graphical example has been implemented in Figure 4.10. It is worthy to note at this point that the only difference between the CC and EC model regarding the 3D results that are obtained from the output angle parameters is that, as the first case builds upon a circular cross-section, the last of the rotations (angle ξ) does not have any effects on the final result.

4.3.3 CCAMMC, ECAMMC and GCS model implementation and results

In this section, the output parameters obtained by means of the analytical models will be analyzed. Thus, a first comparison between the results for MESSENGER and STEREO A will be performed for each case: CCAMMC and ECAMMC. Also, a final comparison between these models and the GCS 3D reconstruction technique will be done.

S/P	ϕ[°]	θ[°]	ξ[°]	δ	y_0[AU]	R_{max}[AU]	ρ
STA CC	157.83	-54.13	90.00	1.00	-0.093	0.137	0.50
MS CC	156.03	9.23	90.00	1.00	-0.040	0.044	0.34
STA EC	141.86	-47.72	90.00	0.69	-0.091	0.164	0.70
MS EC	130.36	23.73	53.08	0.75	-0.040	0.061	0.68

Table 4.3: Set of parameters obtained from the *fitting procedure*: longitude (ϕ), tilt (θ), angle of propagation (ξ), ratio between major and minor ellipse axis' size (δ), closest approach to the flux rope axis (y_0), maximum radius (R_{max}), *fit goodness* (ρ).

In Table 4.3, the parameters for each of the analytical model implementations are enclosed. It is possible to observe that, for the circular-cylindrical case, the longitud (ϕ) seems to be very consistent for both MESSENGER and STA spacecraft. As it has been explained in Section 4.3.2, the parameters ξ and δ do not have any effect for this first case and their value is by default set to 90°and 1, respectively. The tilt angle (θ), however, shows a remarkable difference between both observatories, with -54.13° for the case of MESSENGER and 9.23° for STA. The closest distance to the flux rope axis is negative for both cases, so that the spacecraft would both be crossing the upper part of the structure. An increase in the radius parameter takes place from MESSENGER to STA, which is what would be expected due to the expansion of the ICME. However, the fit goodness (ρ) has a value of 0.50 and 0.34 for each of the observatories which, according to the *success of the reconstructions* classification presented in Section 4.3.1, correspond to a *poor* accuracy of the results.

Thus, taking into account that the performace of the fit for the elliptic-cylindrical analytical implementation offers much more reliable results according to ρ (0.70 and 0.68), the ECAMMC case will be further analyzed in detail in this work. The consistency of the values for ϕ and θ for this case is very similar to the circular-cylindrical alternative, with the longitud offering coherent results and the tilt angle a strong discrepancy between both spacecraft. Now, the angle of propagation (ξ) continues to be 90° for STA, but has a value of 53.08° for MESSENGER, which means that the orientation of the ellipse's major axis in space is modified.

The physical interpretation of these output parameters can be more easily understood from Figures 4.11 and 4.12. These plots show a 3D scale representation of the flux-rope shape obtained by means of the ECAMMC model for both STEREO A and MESSENGER (red and pink elliptic-cylinders, respectively). The GSE coordinate system for the spacecraft has also been included and a black disnotinuous line represents the cylinder's axis final position in space.

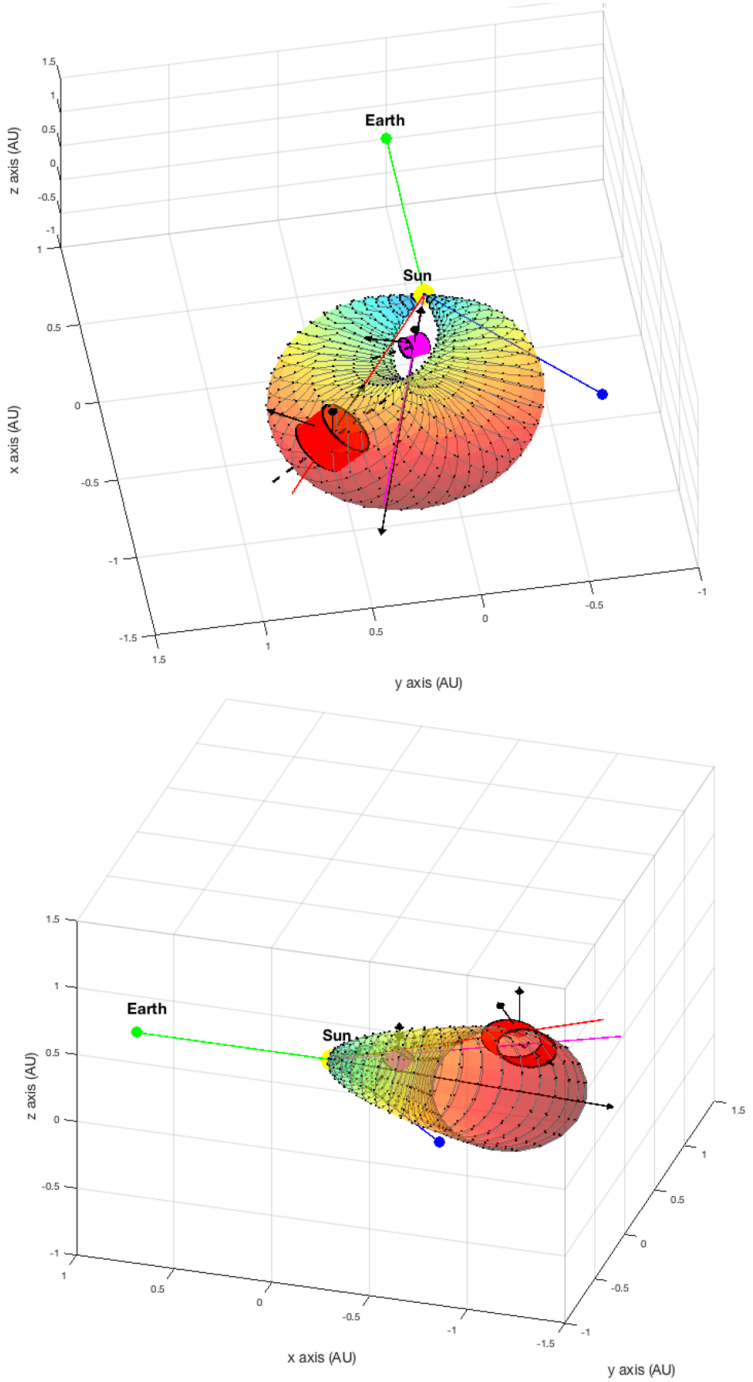

Figure 4.11: 3D scale representation of the position of the Sun, Earth, STA, STB and MESSENGER spacecraft and their corresponding trajectories through the ICME. Also, point cloud representing the ideal shape of the ICME at a distance of 275 Rs from the Sun. Finally, the results obtained after the application of the EC Model in the shape of a red and pink elliptic cylinder are also displayed. *Top row:* view from the top. *Bottom row:* lateral view.

Also, the Earth, Sun, STA, MESSENGER and STB positions have been marked with a green, yellow, red, magenta and blue dots. The point cloud corresponding to the GCS model reconstruction parameters (see Section 4.2.2) projected to $275 R_{Sun}$ has also been added, with different colors along its surface that represent the faster (red) and slower (blue) traveling areas of the ICME. It is worthy to take into account that

this point cloud projection corresponding to the GCS model is just an idealization of the shape of the ICME at $275R_{Sun}$: in reality it has probably undergone a notable distortion, so that the *croissant* shape has been surely lost. The direction of the structure is represented by means of a black arrow. Finally, the spacecraft have been connected to the Sun with a colored line (red: STA, magenta: MESSENGER, blue: STB) to easily observe the intersection points between them and the ICME and clarify the 3D image to the observer.

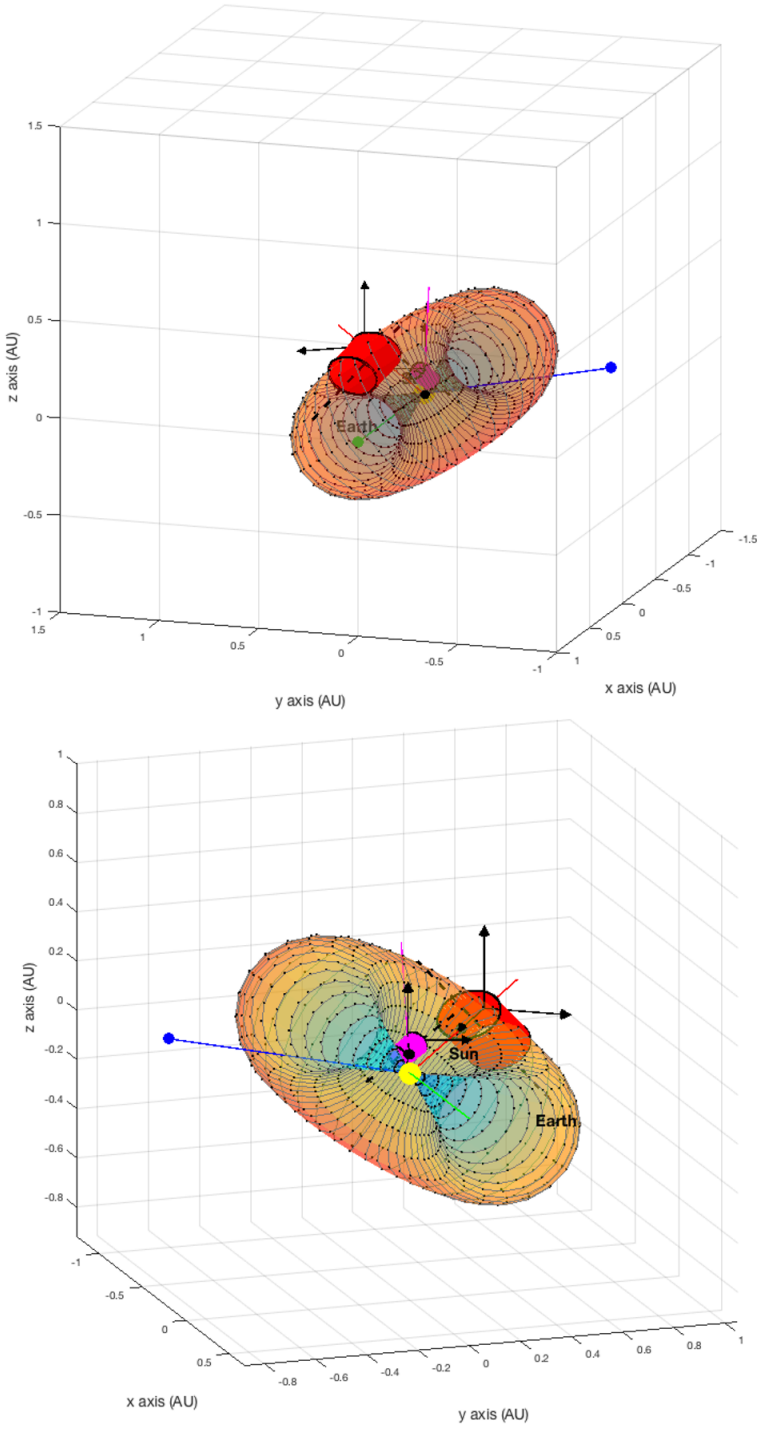

Figure 4.12: Continuation of Fig. 4.11. *Top row:* front view. *Bottom row:* rear end perspective.

In Figures 4.11 and 4.12, it can be seen that the analytical results acquired by means of the ECAMMC for the case of STEREO A are highly coherent with those obtained with the Graduated Cylindrical Shell model within the remote sensing analysis. The tilt angle obtained for the case of MESSENGER, however, highly differs from both the 3D reconstruction orientation of the ICME and STA's tilt angle.

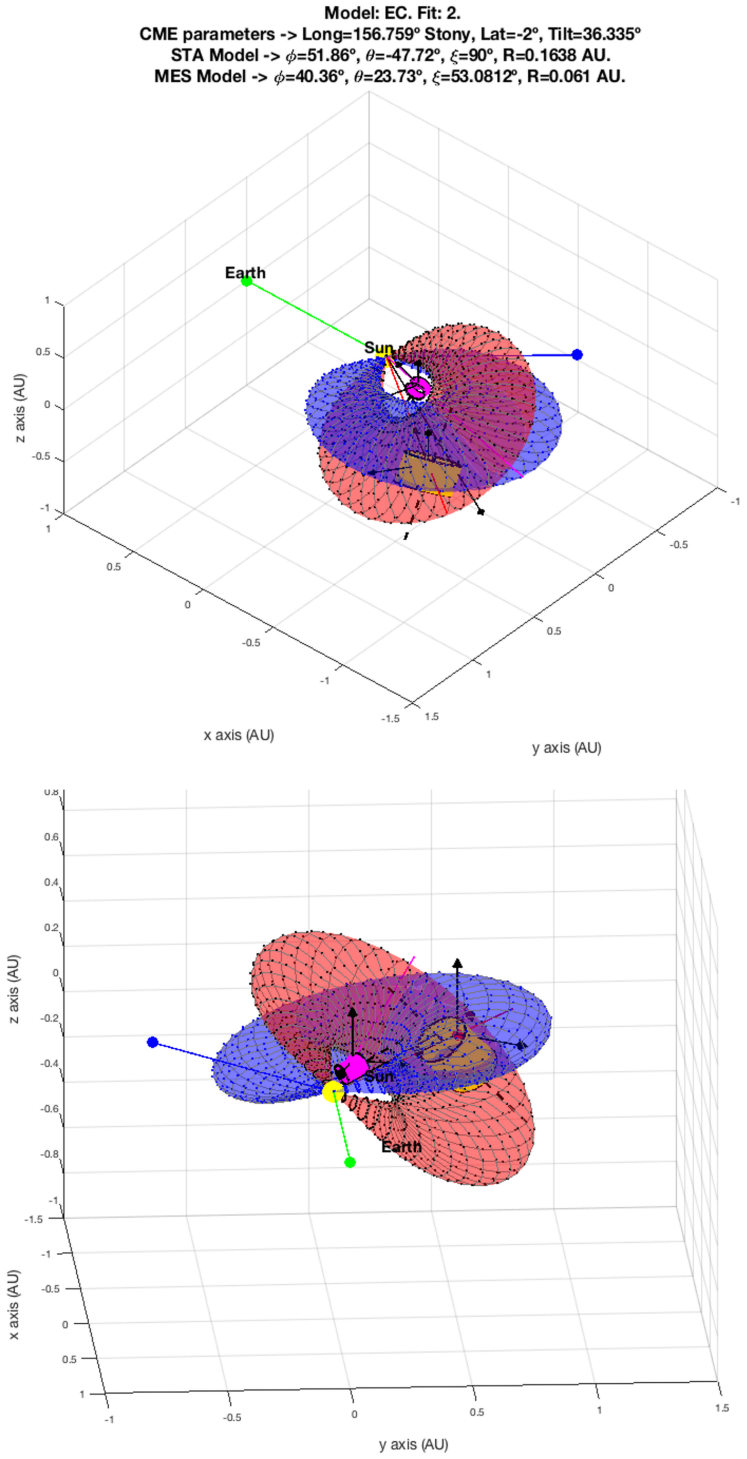

Figure 4.13: Alternative scenario of the event's shape and structure.

There are two main reasons why the discrepancies regarding the tilt angle parameter

among MESSENGER, STA and the ICME may be occuring: a) the reliability of the results obtained by means of the ECAMMC for the case of MESSENGER is not good enough and a higher resolution of measurements points is needed when applying the analytical model technique or b) a second ICME that cannot be easily detected in the images (see Figure 3.10 and 4.8) is being ejected from the Sun, affecting the measurements provided by the MESSENGER observatory. An approximated graphical representation of this second case scenario has been implemented and shown in Figure 4.13.

4.4 Velocity analysis based on GCS model

The arrival time of the ICME at each of the spacecraft MESSENGER and STEREO A is also an important point to be considered when analyzing the robustness and coherence of the results obtained by means of the 3D reconstruction forward model -the Graduated Cylidrical Shell technique, in this case- in contrast with the in-situ measurements. Thus, in this section, the calculation of the intersection points' velocity between the ICME point cloud and the line linking the spacecraft position and the Sun will be performed. This technique allows to obtain the velocity of the ICME's sections of most interest for the purpose of this work in order to evaluate the consistency of the arrival time to both spacecraft that is obtained from the theoretical GCS reconstruction of the structure and the actual time of arrival that is measured when the event actually crosses the observatories (see Table 4.1).

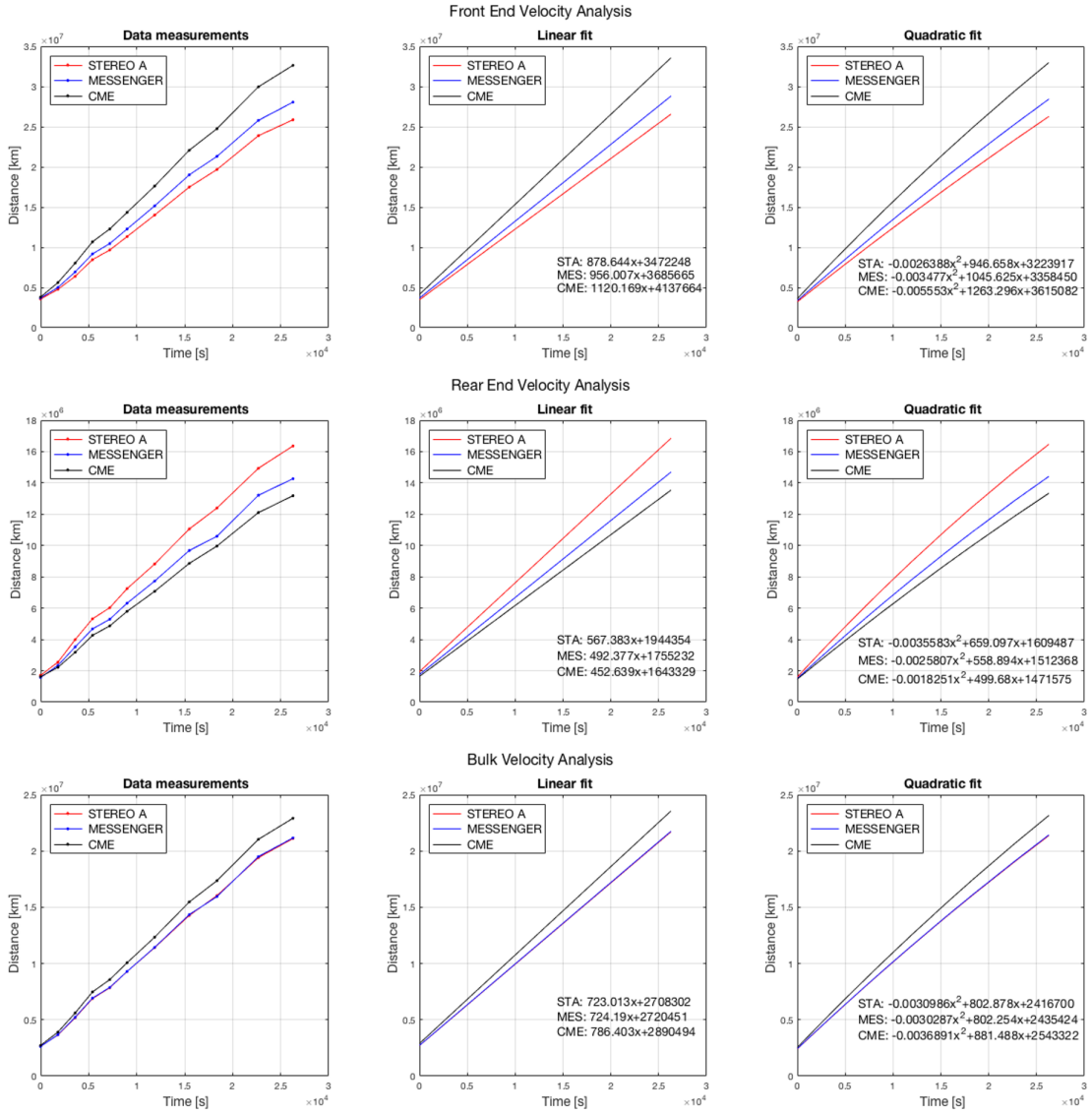

Figure 4.14: ICME velocity analysis: *Top row:* front end speed. *Middle row:* rear end speed. *Bottom row:* bulk speed.

The first step here is to calculate the coordinates of the front end and rear end of the aforementioned intersection points as it can be observed in Figure 4.15; where the red, light blue and dark blue lines correspond to the lines linking STEREO A, MESSENGER and STEREO B with the Sun. The pink and green points correspond to the front and rear end intersection points for both observatories, respectively. The yellow point is obtained from the previous two and is located right at half of the distance between both of them.

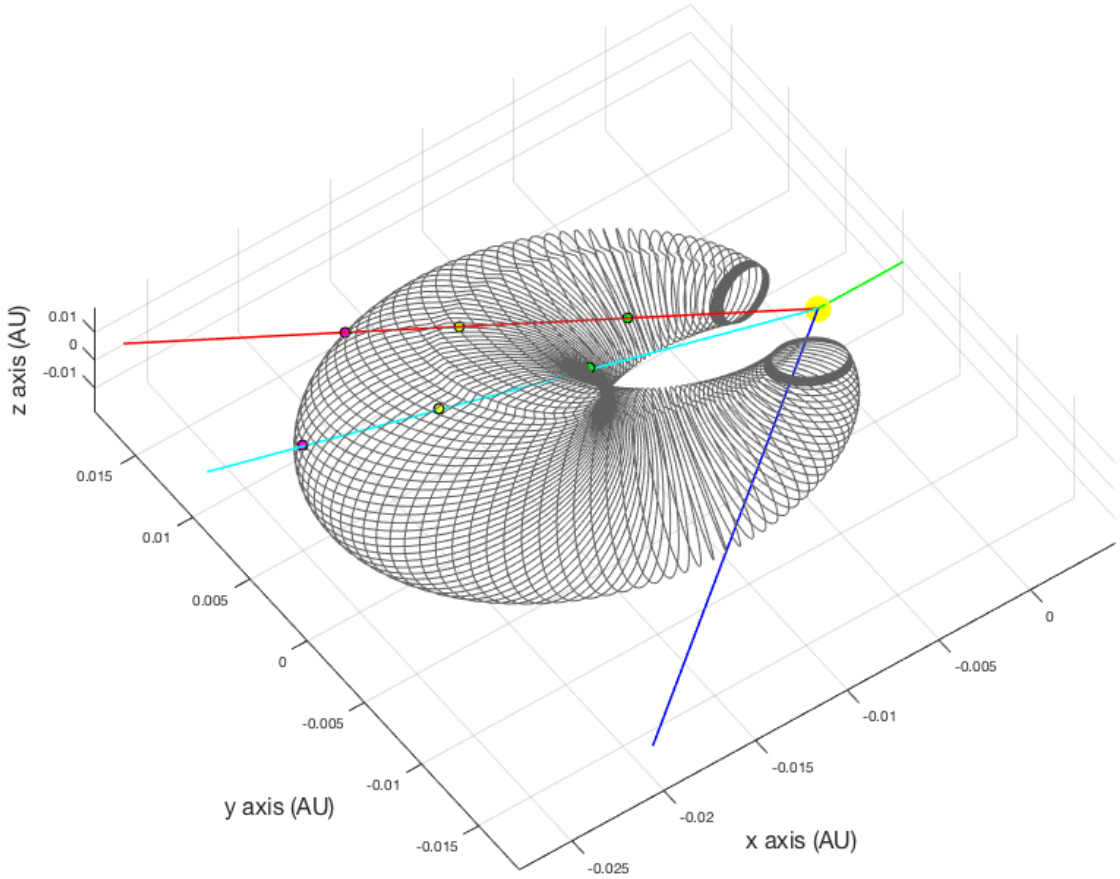

Figure 4.15: Intersection points between the ICME's point cloud (at a height of $5R_{Sun}$) and the line linking the spacecraft STA (red line) and MESSENGER (light blue line) with the Sun.

The same procedure is repeated for each of the GCS reconstruction instants that have been considered (see Table 4.2). Then, a linear and quadratic regression are applied for the front, bulk and read end case and for both of the spacecraft as well, obtaining the results presented in Figure 4.14. However, the speed of the front and read end of the structure is not very representative, as it also contains the expansion velocity. Thus, the bulk velocity must be considered for this analysis as it corresponds to the *true speed* of the ICME.

It can be inferred from these measurements, that the average bulk velocity for STEREO A and MESSENGER taking into account the linear fit presented in Figure 4.14 is 709 km/s for both cases. Thereby, continuing with the linear speed approximation an arrival time of Aug 20, 2013 at 6 pm for MESSENGER and Aug 22, 2013 at 7 am for STEREO A is obtained from the GCS model reconstruction model. Now, comparing with the actual time in which the structure crossed the observato-

ries (see Table 4.1) a difference of only 1 hour for the case of MS is obtained and 16 hours for STA are obtained. Taking into account that an idealization of the shape of the ICME is assumed together with a linear approximation of the bulk velocity, any difference smaller than 24 hours can be taken as a highly consistent result for the analysis. Moreover, taking a look at the quadratic fit for the velocity, it is possible to observe that the quadratic coefficient for the resulting velocity polynomial is negative, which means that the ICME is decelerating.

4.5 ENLIL model discussion and results

ENLIL [15] is a model based on ideal MHD equations that are solved for plasma mass, momentum, energy density and magnetic field that allows to accurately track the trajectory of ICMEs in order to study their extension and arrival time at a certain location in space. Specifically, this model treats the CME as a separate ejecta added to a background solar wind. Thus, it introduces a dense structure with no intrinsic magnetic field and, under certain conditions, it can be very efficient in describing the trajectory of ICMEs. Contemporary versions of ENLIL are commonly driven by the so-called WSA (Wang-Sheeley-Arge) empirical model [1]. The WSA-ENLIL combination is widely used and publicly available at the CCMC web site[1].

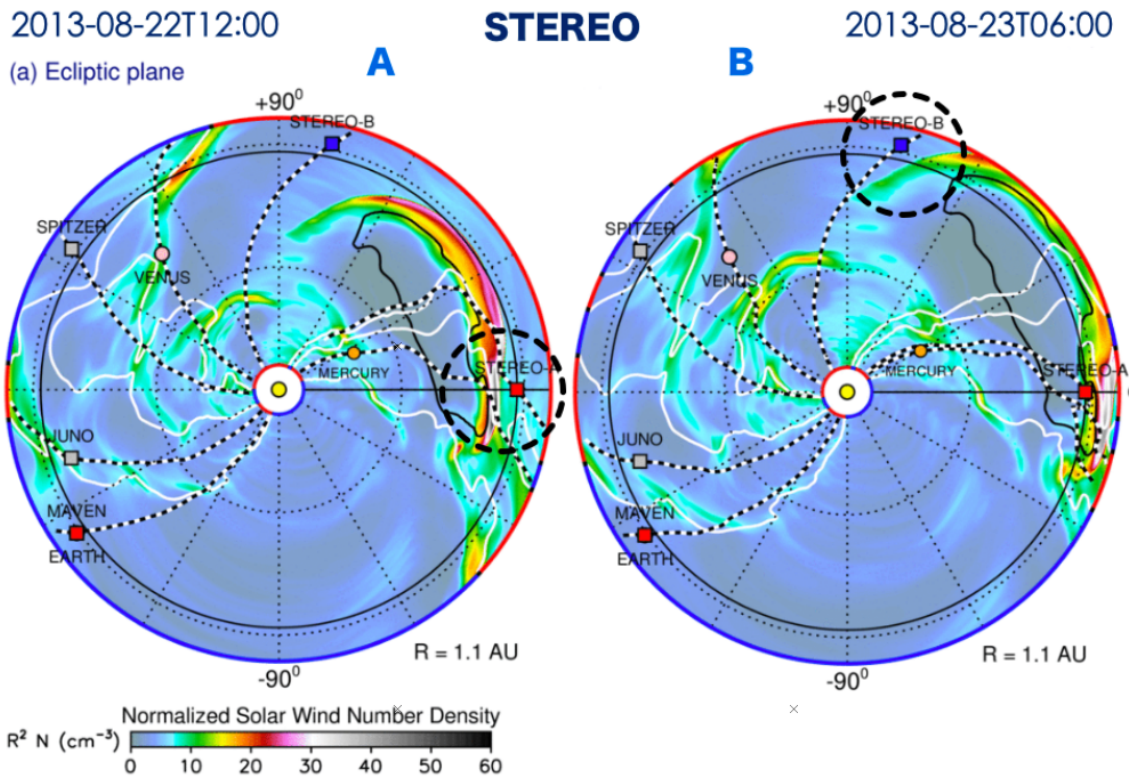

Figure 4.16: ENLIL simulation of the ICME of study observed in August 2013. Shown are solar wind density maps at two different times. The location of the Sun is indicated by the yellow circle, the other planets by red circles and the locations of the Messenger and STEREO spacecraft by the orange, red and blue marks respectively. The ICME is shown as the darker (red, orange, green: high density) structure.

[1] http://ccmc.gsfc.nasa.gov

ENLIL begins with a model of the solar wind and the ICME can be introduced as an over-pressurised plasma cloud in addition to the background. ICME parameters (e.g. location, size, speed) are estimated using models based on coronagraph observations of CMEs: in this case, the parameters derived from the GCS model have been used as an input for this analysis (see Section 4.2.2). The ICME launched as a spherical homogeneous structure, but it becomes distorted as it evolves through the heliosphere. The commonly-used version of ENLIL is therefore actually a combination of three models: WSA feeds the background solar wind parameters,while the GCS model introduces the ICME. Figure 4.16 shows the results for the event of analysis (August 22-23, 2013). ENLIL is a favoured model for ICME modelling and space weather forecasting because of its flexibility and its MHD nature. Also as mentioned above, it performs well in predicting ICME arrival time at a certain location.

The results obtained in previous sections through different models and a comprehensive analysis of the ICME are indeed corroborated in Figure 4.16. Thus, the front of the structure is clearly crossing the STEREO A and MESSENGER spacecraft, so that these observatories allowed to perform the multipoint detection analysis of the event. STEREO B, however, is only crossing the shock of the ICME, as expected.

4.6 Conclusions

In this project, a comprehensive analysis of a very particular event (Aug 2013, DOY 234) was performed after conducting a classification and filtering of the ICME events that took place within the time frame of 2013 to 2014 based on the categorization: flux rope, complex and ejecta. The final structure of study was analyzed both from multipoint observation measurements (in-situ detection by MESSENGER and STEREO) and 3D multi-view reconstruction analysis (images taken by STEREO A and B) in an attempt to help establish a link between in-situ and remote sensing observations.

The in-situ measurements were first described, obtaining a complex structure type for the case of STA and MESSENGER and an ejecta configuration for STB. The forward modelling of the ICME was then implemented by means of the Graduated Cylindrical Shell model to study the three-dimensional shape of the event and its velocity in order to evaluate the consistency between the GCS technique results and the multipoint in-situ observations. Also, the Circular-cylindrical and Elliptic-cylindrical Analytical Flux Rope Model for Magnetic Clouds were applied to the case of study to establish a comparison between in-situ and remote sensing implementations. The ENLIL model was run to verify the assumed hypothesis regarding the evolution of the ICME. Finally, all the different techniques were compared to evaluate the consistency of the analysis.

Part III

Appendix

A | Collection of events and their configuration

This table shows the final classification of events in the years 2013 and 2014 based on the measurements provided by the STEREO spacecraft. The notation used for each configuration type is: a) F: flux rope (+ or -, depending on the degrees of rotation), b) Cx: complex, c) E: ejecta, d) ND: no data.

STEREO A		STEREO B	
2013 009 010/9 02:25	F+		
2013 025 01/25 00:14	F		
2013 039 02/08 07:44	E	2013 039 02/08 08:20	F-
2013 050 02/19 07:44	F	2013 049 02/18 03:06	E
2013 059 02/28 21:14	E		
		2013 066 03/07 12:23	E
2013 067 03/08 02:20			
		2013 083 03/24 05:20	Cx
2013 085 03/26 02:45	F-		
2013 086 03/27 16:09	F-		
		2013 099 04/09 23:40	E
2013 106 04/16 15:36	Cx		
2013 108 04/18 06:10	E		
2013 112 04/22 10:08	E		
2013 117 04/27 04:19	E	2013 117 04/27 01:09	E
2013 117 04/27 23:32	ND		
		2013 118 04/28 19:38	E
2013 122 05/02 21:02	Cx		
		2013 124 05/04 04:52	Cx
		2013 127 05/07 04:37	F
2013 132 05/12 23:30	E		
		2013 135 05/15 13:34	E
		2013 137 05/17 02:54	E
2013 145 05/25 06:05	E		
2013 149 05/29 12:20	Cx		Cx
		2013 153 06/02 06:09	
2013 171 06/20 11:13	F	2013 170 06/19 15:08	Cx
2013 178 06/27 16:17	E		
		2013 186 07/05 07:04	E

2013 195 07/14 23:20	F-		
2013 206 07/25 06:12	Cx		
2013 208 07/27 18:52	F-		
2013 222 08/10 09:16	F+		
2013 234 08/22 07:05	Cx	2013 234 08/22 02:10	E
2013 244 09/01 01:10	E	2013 246 09/03 15:50	E
		2013 252 09/09 14:32	Cx
		2013 258 09/15 16:20	Fr
2013 264 09/21 06:00	E		
2013 277 10/04 04:28	F+		
		2013 281 10/08 04:54	Cx
2013 290 10/17 15:15	Cx		
		2013 294 10/21 18:23	Cx
2013 295 10/22 17:01	Cx		
2013 305 11/01 10:55	E		
2013 308 11/04 08:56	Cx	2013 309 11/05 02:43	Cx
		2013 310 11/06 02:00	F-
		2013 312 11/08 13:28	ND
2013 315 11/11 10:31	F		
2013 317 11/13 17:00	E		
2013 318 11/14 05:50	F-		
2013 322 11/18 18:24	Cx		
2013 330 11/26 19:30	F-	2013 328 11/24 03:22	F
2013 335 12/01 22:29	F+		
		2013 342 12/08 18:22	Cx
		2013 351 12/17 13:29	Cx
		2013 355 12/21 08:25	F-
2013 359 12/25 11:49	F-		
2013 361 12/27 22:22	F-	2013 362 12/28 17:06	ND
2013 365 12/31 13:31	ND	2013 365 12/31 21:47	ND
2014 009 01/09 13:17	Cx		
2014 013 01/13 17:17	Cx		
		2014 025 01/25 02:00	F-
2014 029 01/29 18:13	E	2014 029 01/29 05:20	E
2014 033 02/02 00:18	Cx		
2014 036 02/05 03:27	Cx	2014 036 02/05 16:05	Cx
2014 037 02/06 11:34	F-		
2014 038 02/07 20:59	F-		
2014 047 02/16 07:50	E		
2014 053 02/22 08:00	ND	2014 052 02/21 07:17	ND
2014 053 02/22 23:06	E		
2014 056 02/25 12:15	F-		
2014 058 02/27 20:46	E	2014 059 02/28 04:23	E
		2014 062 03/03 22:00	Cx
2014 066 03/07 18:35	E	2014 067 03/08 04:41	Cx
2014 070 03/11 09:37	F+		
2014 073 03/14 16:37	E	2014 073 03/14 23:10	Cx
		2014 077 03/18 12:00	Cx
2014 089 03/30 21:38	F		

2014 091 04/01 13:30	F-	2014 091 04/01 04:53	E
2014 099 04/09 13:07	F-		
2014 101 04/11 15:24	F-	2014 102 04/12 02:27	F+
		2014 128 05/08 01:37	F
2014 131 05/11 12:33	Cx		
2014 159 06/08 01:44	F		
2014 160 06/09 09:30	F-	2014 160 06/09 01:18	F+
2014 162 06/11 00:14	E		
2014 164 06/13 00:53	F-		
2014 174 06/23 11:00	Cx		
2014 180 06/29 23:30	Cx	2014 178 06/27 18:27	F-
		2014 182 07/01 12:51	Cx
2014 185 07/04 16:53	F		
2014 193 07/12 17:18	ND		
2014 223 08/11 09:03	F	2014 223 08/11 06:20	Cx
2014 243 08/31 02:55	ND	2014 243 08/31 17:45	Cx
2014 246 09/03 13:38	ND	2014 246 09/03 07:45	ND
2014 267 09/24 14:55	ND		
		2014 268 09/25 14:09	ND
2014 289 10/16 20:11	ND		
2014 331 11/27 13:32	ND		
2014 349 12/15 05:38	ND		
2014 356 12/22 10:00	ND		

Table A.1: In-situ characterization of the totality of the events observed by STEREO A and B twin spacecraft between January, 2013 and December, 2014.

Bibliography

[1] C. N. Arge and V. J. Pizzo. Improvement in the prediction of solar wind conditions using near-real time solar magnetic field updates. *Journal of Geophysical Research: Space Physics*, 2008.

[2] L. Burlaga, E. Sittler, F. Mariani, and R. Schwenn. Magnetic loop behind an interplanetary shock: Voyager, Helios, and IMP 8 observations. *Journal of Geophysical Research*, 2008.

[3] M. A. Hidalgo, C. Cid, J. Medina, and A. F. Viñas. A new model for the topology of magnetic clouds in the solar wind. *Solar Physics*, 2000.

[4] M. A. Hidalgo, C. Cid, A. F. Viñas, and J. Sequeiros. A non-force-free approach to the topology of magnetic clouds in the solar wind. *Journal of Geophysical Research: Space Physics*, 2002.

[5] R A Howard, N R Jr Sheeley, D J Michels, and M J Koomen. Coronal mass ejections - 1979-1981. *Journal of Geophysical Research*, 1985.

[6] Timothy. Howard. *Coronal mass ejections: An Introduction*. Springer, 2011.

[7] L. Jian, C. T. Russell, J. G. Luhmann, and R. M. Skoug. Properties of interplanetary coronal mass ejections at one AU during 1995 - 2004. *Solar Physics*, 2006.

[8] R. P. Lepping, D. B. Berdichevsky, C. C. Wu, A. Szabo, T. Narock, F. Mariani, A. J. Lazarus, and A. J. Quivers. A summary of WIND magnetic clouds for years 1995-2003: Model-fitted parameters, associated errors and classifications. *Annales Geophysicae*, 2006.

[9] R.P. P. Lepping, L.F. F. Burlaga, J.a. a. Jones, and L.F. F. Burlaga. Magnetic field structure of interplanetary magnetic clouds at 1 AU. *Journal of Geophysical Research*, 95(A8):11,957–11,965, 1990.

[10] Ying Liu, Arnaud Thernisien, Janet G. Luhmann, Angelos Vourlidas, Jackie A. Davies, Robert P. Lin, and Stuart D. Bale. Reconstructing coronal mass ejections with coordinated imaging and in situ observations: Global structure, kinematics, and implications for space weather forecasting. *Astrophysical Journal*, 2010.

[11] NASA. Official STEREO Mission Website. https://stereo.gsfc.nasa.gov/.

[12] T. Nieves-Chinchilla, R. Colaninno, A. Vourlidas, A. Szabo, R. P. Lepping, S. A. Boardsen, B. J. Anderson, and H. Korth. Remote and in situ observations of an

unusual Earth-directed coronal mass ejection from multiple viewpoints. *Journal of Geophysical Research: Space Physics*, 2012.

[13] T. Nieves-Chinchilla, M. G. Linton, M. A. Hidalgo, A. Vourlidas, N. P. Savani, A. Szabo, C. Farrugia, and W. Yu. A CIRCULAR-CYLINDRICAL FLUX-ROPE ANALYTICAL MODEL FOR MAGNETIC CLOUDS. *The Astrophysical Journal*, 2016.

[14] T. Nieves-Chinchilla, A. Vourlidas, J. C. Raymond, M. G. Linton, N. Al-haddad, N. P. Savani, A. Szabo, and M. A. Hidalgo. Understanding the Internal Magnetic Field Configurations of ICMEs Using More than 20 Years of Wind Observations. *Solar Physics*, 2018.

[15] D. Odstrcil, P. Riley, J. A. Linker, R. Lionello, Z. Mikic, and V. J. Pizzo. 3-D simulations of ICMEs by coupled coronal and heliospheric models. In *European Space Agency, (Special Publication) ESA SP*, 2003.

[16] Watanachak Poomvises, Jie Zhang, and Oscar Olmedo. CORONAL MASS EJECTION PROPAGATION AND EXPANSION IN THREE-DIMENSIONAL SPACE IN THE HELIOSPHERE BASED ON STEREO /SECCHI OBSERVATIONS . *The Astrophysical Journal*, 2010.

[17] W. H. Press, B. P. Flannery, and S. A. Teukolsky. *Numerical Recipes in Fortran 77. The Art of Scientific Computing*. 1986.

[18] A. P. Rouillard, J. A. Davies, R. J. Forsyth, N. P. Savani, N. R. Sheeley, A. Thernisien, T. L. Zhang, R. A. Howard, B. Anderson, C. M. Carr, S. Tsang, M. Lockwood, C. J. Davis, R. A. Harrison, D. Bewsher, M. Fränz, S. R. Crothers, C. J. Eyles, D. S. Brown, I. Whittaker, M. Hapgood, A. J. Coates, G. H. Jones, M. Grande, R. A. Frahm, and J. D. Winningham. A solar storm observed from the Sun to Venus using the STEREO, Venus Express, and MESSENGER spacecraft. *Journal of Geophysical Research: Space Physics*, 2009.

[19] A. Thernisien. Implementation of the graduated cylindrical shell model for the three-dimensional reconstruction of coronal mass ejections. *Astrophysical Journal, Supplement Series*, 2011.

[20] A. Thernisien, A. Vourlidas, and R. A. Howard. Forward modeling of coronal mass ejections using STEREO/SECCHI data. *Solar Physics*, 2009.

[21] A. F. R. Thernisien, R. A. Howard, and A. Vourlidas. Modeling of Flux Rope Coronal Mass Ejections. *The Astrophysical Journal*, 2006.

[22] B. E. Wood and R. A. Howard. An empirical reconstruction of the 2008 april 26 coronal mass ejection. *Astrophysical Journal*, 2009.

[23] Thomas H. Zurbuchen and Ian G. Richardson. In-situ solar wind and magnetic field signatures of interplanetary coronal mass ejections. *Space Science Reviews*, 2006.